Article

Neuron

Cholinergic Sensorimotor Integration Regulates Olfactory Steering

Highlights

- Sensorimotor integration regulates goal-directed behavioral tasks
- Two cholinergic signals encode sensory and motor information
- Sensory and motor cholinergic signals interact to generate integration
- Experience-dependent changes in sensorimotor integration

Authors

He Liu, Wenxing Yang, Taihong Wu, Fengyun Duan, Edward Soucy, Xin Jin, Yun Zhang

Correspondence

yzhang@oeb.harvard.edu

In Brief

Liu et al. show that during olfactory steering, two different cholinergic signals representing the motor state and the sensory response integrate in a *C. elegans* interneuron to decode the spatial information of the odorant and steer the locomotory trajectory.

Liu et al., 2018, Neuron *97*, 390–405
January 17, 2018
https://doi.org/10.1016/j.neuron.2017.12.003

CellPress

CellPress

Neuron
Article

Cholinergic Sensorimotor Integration Regulates Olfactory Steering

He Liu,[1,2] Wenxing Yang,[1,2] Taihong Wu,[1,2] Fengyun Duan,[1,2] Edward Soucy,[2] Xin Jin,[3] and Yun Zhang[1,2,4,*]
[1]Department of Organismic and Evolutionary Biology
[2]Center for Brain Science
[3]Society of Fellows
Harvard University, Cambridge, MA 02138, USA
[4]Lead Contact
*Correspondence: yzhang@oeb.harvard.edu
https://doi.org/10.1016/j.neuron.2017.12.003

SUMMARY

Sensorimotor integration regulates goal-directed movements. We study the signaling mechanisms underlying sensorimotor integration in *C. elegans* during olfactory steering, when the sinusoidal movements of the worm generate an in-phase oscillation in the concentration of the sampled odorant. We show that cholinergic neurotransmission encodes the oscillatory sensory response and the motor state of head undulations by acting through an acetylcholine-gated channel and a muscarinic acetylcholine receptor, respectively. These signals converge on two axonal domains of an interneuron RIA, where the sensory-evoked signal suppresses the motor-encoding signal to transform the spatial information of the odorant into the asymmetry between the axonal activities. The asymmetric synaptic outputs of the RIA axonal domains generate a directional bias in the locomotory trajectory. Experience alters the sensorimotor integration to generate specific behavioral changes. Our study reveals how cholinergic neurotransmission, which can represent sensory and motor information in the mammalian brain, regulates sensorimotor integration during goal-directed locomotions.

INTRODUCTION

Cue-guided movements are essential for animals to locate food, find a mate, or catch prey, during which the sensory response and the motor state often regulate each other. The movement generated by an animal can shape the spatial and the temporal pattern of the sensory response, which is processed to modulate the ongoing movement. For example, when a honeybee executes a smooth landing toward food, the angular speed of the retinal image of the ground depends on the flying speeds in the forward and the descending directions. To avoid colliding with the ground, the flying speeds in both directions are adjusted to keep the angular speed of the ground image constant (Srinivasan, 2011). Similarly, when searching for prey a weakly electrical fish swims with a body pitch angle that optimizes the volume of the water sampled, but when catching the prey the fish reduces the swimming pitch angle to minimize the sensory noise resulting from its own movements (MacIver et al., 2001; von der Emde et al., 2008). Thus, the continuous interaction between sensory system and motor system allows the nervous system to effectively sample the relevant sensory information from the environment and to regulate the behavioral output in order to reach the goal defined by the sensory system. Furthermore, sensorimotor integration also plays important roles in signal processing in the central nervous system. For example, mammals often use sniffing to detect an odorant or distinguish between different odorants. The rhythmic inhalation and exhalation of the air flow generated by sniffing produces an oscillation in the concentration of the odorant sampled by the nose (Karpov, 1980; Laing, 1986; Welker, 1964), which is temporally coupled to the sensory response of olfactory processing neurons, providing a potential mechanism for encoding the identity and concentration of the odorants (Kepecs et al., 2006).

While these previous studies demonstrate the reciprocal modulation of sensory input and behavioral output during sensorimotor integration, the underlying molecular and cellular mechanisms are largely unknown. In the mammalian central nervous system, cholinergic neurotransmission has been implicated in sensorimotor integration. The cholinergic neurons in the basal forebrain regulate various cognitive functions and integrate sensory processing with the internal state, such as arousal or attention (Ballinger et al., 2016; Hasselmo and Sarter, 2011). The basal forebrain cholinergic neurons project into diverse brain regions, including the visual and auditory cortices, as well as the hippocampus and the amygdala (Ballinger et al., 2016 and the references therein). The cholinergic terminals in the sensory cortices can transmit signals that are associated with the motor state (Eggermann et al., 2014; Fu et al., 2014; Lee et al., 2014; Nelson and Mooney, 2016). For example, the activity of the basal forebrain-derived cholinergic axons in the auditory cortex can be related to the ongoing movements, including a rhythmic explorative movement whisking, and modulates the auditory sensory responses (Nelson and Mooney, 2016). Meanwhile, the basal forebrain cholinergic terminals in the prefrontal cortex can respond to sensory cues

(Howe et al., 2013; Parikh et al., 2007). These findings reveal the function of cholinergic neurotransmission in representing various sensory and motor signals.

Here, we use *Caenorhabditis elegans* to characterize the molecular, neuronal, and circuit mechanisms of sensorimotor integration during a goal-directed locomotory task, olfactory steering. *C. elegans* moves on a solid substrate by generating a dorsal-ventral sinusoidal body wave that propagates along the body (Wen et al., 2012). *C. elegans* performs chemotaxis toward attractive odorants and salts by regulating the frequency of reversals and turns or by generating a gradually curved steering trajectory toward the attractants, such as the odorant isoamyl alcohol (IAA) (Albrecht and Bargmann, 2011; Bargmann et al., 1993; Bargmann and Horvitz, 1991; Iino and Yoshida, 2009; Pierce-Shimomura et al., 1999). When steering toward IAA, the oscillatory dorsal-ventral head undulations allow AWC, the head chemosensory neuron that detects IAA (Bargmann et al., 1993; White et al., 1986), to sample the IAA concentration within the space of head swings. This sampling movement shapes the concentration of IAA detected by AWC into cycles of rise and fall that oscillate at the speed of the head undulations. Meanwhile, AWC generates in-phase responses to IAA pulses that oscillate as rapidly as the head swings (Kato et al., 2014). While the rapid temporal dynamics of the AWC response are important for steering toward IAA, how the oscillatory sensory input integrates with the motor state of the head undulations to modulate steering is not understood. In addition, the worm can steer toward IAA that is spatially located either on the ventral or the dorsal side of its body. How the spatial information of the odorant is processed to modulate the direction of steering toward the cue has not been addressed.

Here, we show that *C. elegans* integrates the information of its own motor state, the dorsal versus the ventral head undulation, with the sensory response to the oscillatory odorant concentrations in the central neural circuit to regulate sensorimotor decisions that direct the steering movements toward the attractive odorant IAA. We find that signaling through a conserved muscarinic cholinergic receptor and an acetylcholine-gated chloride channel represents the motor information and the sensory information, respectively, to generate sensorimotor integration in the axon of an interneuron through an inhibitory interaction. The sensorimotor integration produces an asymmetry in the activities of the two axonal domains of the interneuron and the asymmetric synaptic outputs of the axonal domains bias the locomotory trajectory. Furthermore, we show that experience modulates the sensorimotor integration to generate odorant-specific changes in the steering movements.

RESULTS

The Interneuron RIA Regulates Olfactory Steering

C. elegans moves forward on a surface by generating a sinusoidal body wave on the dorsal-ventral plane (Wen et al., 2012). We recorded individual worms that steered toward IAA using a camera with a high pixel density (STAR Methods). First, we quantified the curving angle, which was the change of the locomotory direction during the steering (Iino and Yoshida, 2009; Izquierdo and Lockery, 2010; Kato et al., 2014; Figure S1A). We measured the curving angle generated over each half head undulation, when an animal swung its head between the most ventral positon and the most dorsal position. We examined the curving angle and the bearing angle, which was the direction of the locomotory trajectory relative to the direction of the odorant (Figure S1A). Consistent with previous studies, we found that the curving angle formed a sinusoidal curve when the bearing angle ranged from 0° to 180°. The curving angle displayed the largest value when the bearing angle was around 90°, indicating that the largest steering toward IAA occurs when the locomotory direction is around perpendicular to the direction of the odorant (Figure S1B).

Next, to quantify the efficiency of olfactory steering, we used the navigation index, which was defined as the radial speed toward the end point of the steering on the edge of the IAA drop (V_r) divided by the traveling speed along the steering trajectory (V_t) (Luo et al., 2014). The most or the least efficient steering occurs when a worm travels directly toward or away from IAA, respectively (Figure 1A). We tested a series of IAA concentrations and found that the navigation index fell significantly when the IAA concentration decreased (Figure 1B). Consistently, the total distance that a worm traveled during steering significantly increased with the lower concentrations of IAA (Figure 1C). We also found that the navigation index decreased significantly when the distance between the starting point of the worm and the position of the IAA drop increased (Figure S1C). These results indicate that the efficiency of olfactory steering depends on the concentration of the odorant.

We then characterized olfactory steering by examining the interneuron RIA, which is synaptically connected with the olfactory sensory circuit and the motor circuit (Hendricks et al., 2012; White et al., 1986; Figure 1D). Using transgenic animals that selectively expressed the tetanus toxin (Schiavo et al., 1992) in RIA with a cell-specific promoter *glr-3* (Brockie et al., 2001) to block its synaptic release (*RIA::TeTx*), we found that the transgenic animals displayed a significantly smaller navigation index (Figure 1E) and traveled a longer distance before reaching IAA (Figure 1F) in comparison with wild-type. Meanwhile, the average duration of one head undulation was not altered by expressing the tetanus toxin in RIA (Figure 1G). Together, these results demonstrate that the interneuron RIA is involved in olfactory steering.

The Sensory Response of RIA Displays the Dynamics of Head Undulations

RIA has a single unbranched axon. The loop-shaped proximal axonal region contains the postsynaptic sites that receive information from several sensory neurons and upper-layer interneurons. The ring-shaped distal axonal region contains the ventral (nrV) and the dorsal (nrD) domains that synaptically and reciprocally connect with the dorsal and the ventral pair of the SMD head motor neurons, SMDD and SMDV (White et al., 1986; Figure 1D). The activity of SMDD and SMDV correlates with the dorsal and the ventral head bending, respectively, and regulates the amplitude of the dorsal-ventral head undulations during sinusoidal movements (Gray et al., 2005; Hendricks et al., 2012; Kato et al., 2015; Nguyen et al., 2016; Shen et al., 2016; Venkatachalam et al., 2016). Using intracellular calcium imaging

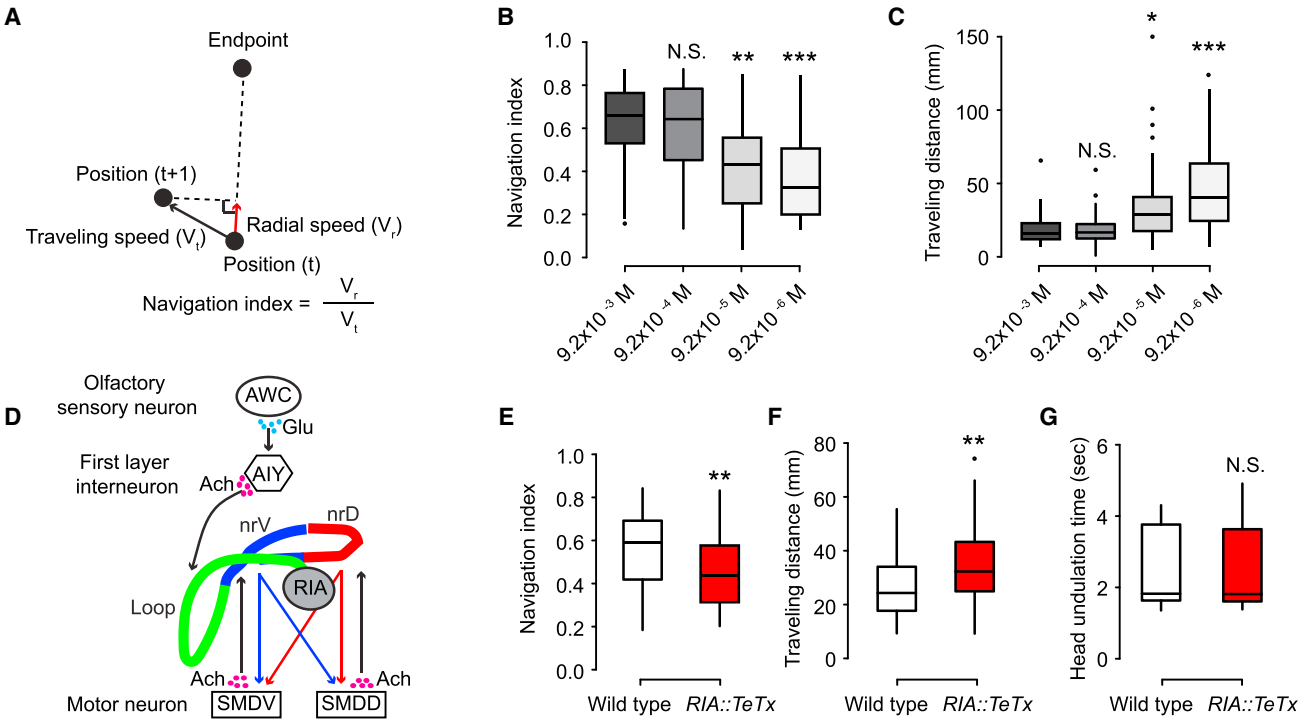

Figure 1. The Interneuron RIA Is Involved in Olfactory Steering in *C. elegans*

(A) Schematics for the navigation index during steering toward an attractive odorant. The end point of steering is on the edge of the drop of the odorant source.

(B and C) Navigation index decreases (B) and traveling distance before reaching isoamyl alcohol (IAA) increases (C) when animals steer toward decreasing concentrations of IAA. n = 30 (9.2×10^{-3} M), 29 (9.2×10^{-4} M), 34 (9.2×10^{-5} M), and 23 (9.2×10^{-6} M) animals, one-way ANOVA.

(D) Schematics showing the sensory and motor circuits that anatomically converge on the axon of RIA. Arrows denote synapses (White et al., 1986); the RIA soma, nrV, nrD, and loop axonal domains are highlighted with colors; and the synaptic outputs of nrV and nrD are highlighted with blue and red, respectively. The characterized neurotransmitters in the circuits are shown. Glu, glutamate; Ach, acetylcholine.

(E and F) Selectively blocking the synaptic release of RIA by expressing the tetanus toxin (TeTx) reduces the navigation index (E) and increases the total traveling distance (F) when steering toward IAA (9.2×10^{-3} M). n = 47 wild-type, n = 53 *RIA::Tetx* transgenic animals, Student's t test.

(G) Expressing the tetanus toxin in RIA does not alter the average duration of one head undulation. n = 16 wild-type, n = 22 *RIA::TeTx* transgenic animals, Student's t test.

***p < 0.001, **p < 0.01, *p < 0.05; N.S., not significant. The boxplots show the first quartile, median, and third quartile; the whiskers extend to the data points that are equal to or less than 1.5 IQR (interquartile range) away from the first or the third quartile; dots are outliers.

See also Figure S1.

with a microfluidic chip, which confines a worm in a channel with the head freely bending in the dorsal-ventral direction in a fluidic stream (Chronis et al., 2007), previous studies show that the activities of the nrV and the nrD axonal domains of RIA correlate with the ventral and the dorsal head bendings, respectively, and that the motor-encoding activity depends on the synaptic outputs of the SMD motor neurons. Meanwhile, stimulating the worm with IAA evokes synchronous calcium responses in the loop, the nrV and the nrD domains of RIA (Hendricks et al., 2012; Jin et al., 2016). These findings show that RIA generates compartmentalized axonal activity to encode the motor state of head bending and synchronous activity to represent sensory information, suggesting a potential function of RIA in sensorimotor integration (Hendricks et al., 2012; Hendricks and Zhang, 2013). We hypothesize that RIA integrates the sensory response and the motor state to steer the undulatory movements toward the attractive odorant.

When steering toward IAA, the head of a worm undulates in the dorsal-ventral direction, which results in an oscillation in the IAA concentration sampled by the head sensory neuron AWC (Izquierdo and Lockery, 2010; Kato et al., 2014). If RIA integrates the sensory response with the state of head undulations to regulate steering, we predict that RIA is able to respond to an oscillatory olfactory input that has a temporal pattern of the head undulations. To probe the dynamics of the sensory response in RIA, we stimulated the transgenic animals that expressed GCaMP3 in RIA with 1 s on and 1 s off pulses of IAA in a microfluidic chip. We used the IAA pulses at 0.5 Hz because the frequency of the head undulations during the steering was about 0.5 Hz under the experimental conditions (STAR Methods; Figure 1G). Although a worm in the microfluidic chip bends its head with less regular durations and intervals than a freely moving worm (Figure 2A), using the chip allows us to deliver the olfactory cue with a defined frequency, which facilitates the identification of the sensory response of RIA. We found that the GCaMP signals of nrV and nrD displayed two temporal patterns (Figure 2A; Movie S1). One correlated with the head bendings in the ventral-dorsal direction (Figure 2B), consistent

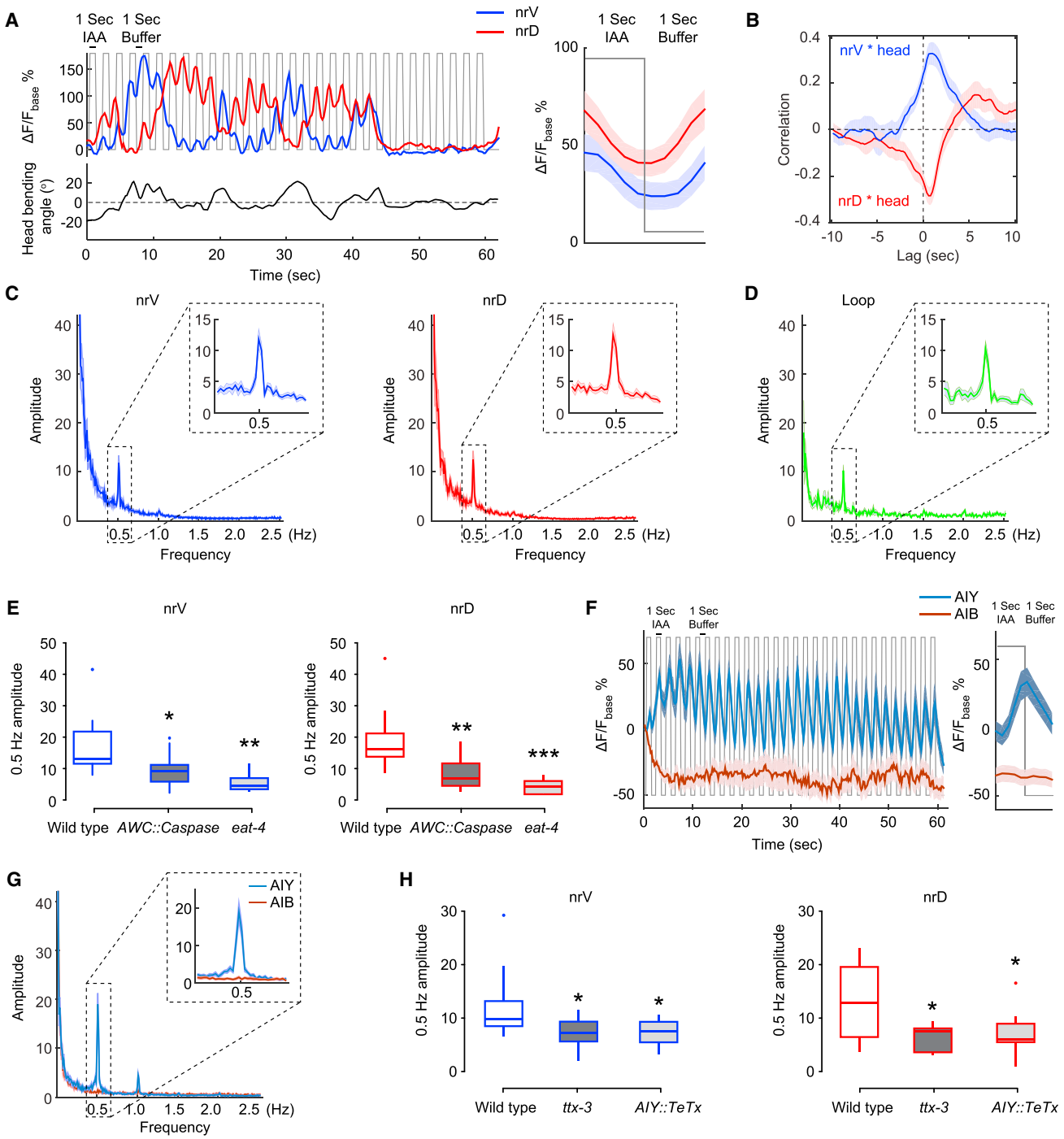

Figure 2. RIA Responds to the Pulses of Olfactory Stimulation as Rapidly as the Head Undulates

(A) Sample traces for the GCaMP3 signals of the nrV and the nrD axonal domains of RIA and the head bending angles of one worm that is stimulated with 0.5 Hz pulses of isoamyl alcohol (IAA, 9.2×10^{-3} M) in a microfluidic chip (left panel) and the average GCaMP3 signals per stimulation cycle for the trace in the left panel (right panel; solid lines represent mean; shades represent SEM). F_{base} is the mean intensity of the axonal signals in a few frames of low-activity state; ΔF indicates $F - F_{base}$.

(B) Cross-correlation between the RIA axonal GCaMP3 signals and the head bendings in a microfluidic chip. Ventral direction is positive, solid lines represent mean, and shades represent SEM, n = 8 animals.

(C and D) Samples of the Fourier transforms of the GCaMP3 signals of nrV (C; n = 15 animals), nrD (C; n = 15 animals), or loop (D; n = 7 animals) domains of RIA show the peak at 0.5 Hz, which is the frequency of IAA stimulation. Solid lines represent mean; shades represent SEM.

(legend continued on next page)

with previous findings (Hendricks et al., 2012). The second was a rapid wave of activity that was phase-locked with the IAA pulses and temporally synchronous between nrV and nrD (Figure 2A). Both nrV and nrD domains responded to the onset and the removal of IAA with decreased and increased GCaMP signals, respectively (Figure 2A). In the later part of the recording, the worm in Figure 2A did not bend its head. We used the Fourier transform to analyze the temporal patterns of the GCaMP signals. The analysis identified a peak at the frequency of 0.5 Hz, which was the frequency of the IAA pulses, in the signals of nrV and nrD (Figure 2C). The GCaMP signal in the loop domain that contained the postsynaptic sites of the sensory pathway responded to the IAA pulses with the same frequency and direction (Figures 2D and S2A). Meanwhile, because the head bending occurred with variable rates and durations in the chip, the Fourier transform did not identify a peak correlated with head bending (Figure 2C). In the absence of the IAA stimulation, the GCaMP signals of nrV or nrD produced no detectable peak at 0.5 Hz when analyzed with the Fourier transform (Figure S2B). These results demonstrate that the RIA axonal domains generate the sensory-evoked synchronous activity as rapidly as the head undulates during olfactory steering.

Next, we sought the sensory circuit underlying the IAA-evoked synchronous GCaMP signals in RIA. Previous studies show that the AWC sensory neuron generates in-phase responses to IAA pulses (Kato et al., 2014). AWC uses glutamate to transmit olfactory responses to the downstream circuit (Chalasani et al., 2007). We found that a deletion mutation in *eat-4*, which encoded a vesicular glutamate transporter (Lee et al., 2008), abolished the synchronous response of RIA to the 0.5 Hz IAA pulses (Figure 2E). Killing AWC by selectively expressing a cell-death-promoting caspase in AWC (Beverly et al., 2011) strongly reduced the amplitude of the 0.5 Hz peak in the Fourier transform of the sensory response of nrV and nrD (Figure 2E). Thus, AWC and the glutamatergic neurotransmission mediate the rapid synchronous sensory response of RIA. AWC transmits olfactory responses to the postsynaptic interneurons AIY and AIB (Chalasani et al., 2007), which synaptically connect with the loop domain of the RIA axon (White et al., 1986). Using intracellular calcium imaging (STAR Methods), we found that when stimulated with 0.5 Hz pulses of IAA, AIY generated an increased calcium signal in response to the onset of IAA and that, similar to the sensory response in RIA, the calcium signal in AIY was phase-locked with the IAA pulses (Figure 2F; Movie S2) and the Fourier transform of the AIY calcium signals produced a strong peak at 0.5 Hz (Figure 2G). Although the worms bent the head irregularly in the chip, the sensory response of AIY was robust. In contrast, the interneuron AIB did not generate an oscillatory response to 0.5 Hz pulses of IAA (Figures 2F and 2G), consistent with a slower temporal property of the AIB activity (Gordus et al., 2015). Blocking the synaptic neurotransmission from AIY by selectively expressing the tetanus toxin in AIY with a *ttx-3* promoter (Hobert et al., 1997) disrupted the synchronous response of RIA to the IAA pulses (Figure 2H). A mutation in *ttx-3*, which encoded a LIM homeodomain-containing transcription factor required for the development and function of AIY (Hobert et al., 1997), similarly reduced the responses of RIA to the IAA pulses (Figure 2H). These results identify the sensory neuron AWC and the first-layer interneuron AIY as a main circuit for the synchronous sensory response of RIA and indicate that similar to AWC, both AIY and RIA respond to oscillatory olfactory simulation with a temporal pattern that matches the dynamics of the head undulations during steering movements.

Cholinergic Neurotransmission Regulates the Sensory-Evoked and the Motor-Encoding Activities of RIA

To understand how the RIA axonal domains simultaneously generate the sensory-evoked and the motor-encoding activities, we sought the underlying neurotransmissions. We first examined a loss-of-function mutation, *gk305*, in *gar-3*, which encoded a G protein-coupled muscarinic acetylcholine receptor (Park et al., 2003). Previous studies show that GAR-3 acts in RIA to generate the compartmentalized RIA axonal activity that encodes head bendings. In the *gar-3(gk305)* mutant animals, RIA no longer exhibits the head bending-correlated activity and the activities of the nrV and the nrD axonal domains become synchronous (Hendricks et al., 2012). We stimulated the *gar-3(gk305)* mutant animals with 0.5 Hz pulses of IAA in a microfluidic chip and quantified the sensory-evoked synchronous GCaMP signals in nrV and nrD. As previously demonstrated, the RIA axonal domains in the *gar-3* mutant animals lost the motor-encoding activities (Figure 3A), which was indicated by the loss of the correlation between the intensity of the axonal GCaMP signals and the amplitude of the head bendings (Figures 3B and S3A). However, the RIA axonal domains in the *gar-3* animals continued to generate the synchronous response to the IAA pulses that was phase-locked with the temporal pattern of the IAA stimulation (Figure 3A). The amplitudes of the 0.5 Hz peaks identified by the Fourier transform of the GCaMP signals of nrV and nrD were comparable in wild-type, the *gar-3* mutant animals, and

(E) Genetic ablation of AWC neuron (*AWC::Caspase*, n = 12 animals) or mutating *eat-4* (n = 8 animals) significantly reduces the amplitudes of the 0.5 Hz peak identified by the Fourier transform of the nrV and the nrD GCaMP3 signals in RIA in comparison with wild-type (n = 12 animals). One-way ANOVA; the boxplots show the first quartile, median, and third quartile; the whiskers extend to the data points that are equal to or less than 1.5 IQR away from the first or the third quartile; dots are outliers.

(F and G) Mean traces of the GCaMP6 signals (left panel, F) in the interneurons AIY (n = 15 animals) and AIB (n = 14 animals) in response to 0.5 Hz pulses of IAA (9.2×10^{-3} M) and the average GCaMP6 signals per stimulation cycle for the traces in the left panel (right panel, F; n, number of worms), and the Fourier transforms of the GCaMP6 signals (G). Solid lines represent mean; shades represent SEM. F_{base} is the mean intensity during the 2 s window before the first onset of IAA; ΔF indicates $F - F_{base}$.

(H) Mutating *ttx-3* (n = 11 animals) or blocking the synaptic release from AIY (*AIY::TeTx,* n = 11 animals) significantly reduces the amplitude of the 0.5 Hz peak identified by the Fourier transform of the GCaMP3 signals of nrV and nrD evoked by 0.5 Hz IAA pulses in comparison with wild-type (n = 15 animals). One-way ANOVA; the boxplots show the first quartile, median, and third quartile; the whiskers extend to the data points that are equal to or less than 1.5 IQR away from the first or the third quartile; dots are outliers.

***p < 0.001, **p < 0.01, *p < 0.05. See also Figure S2 and Movies S1 and S2.

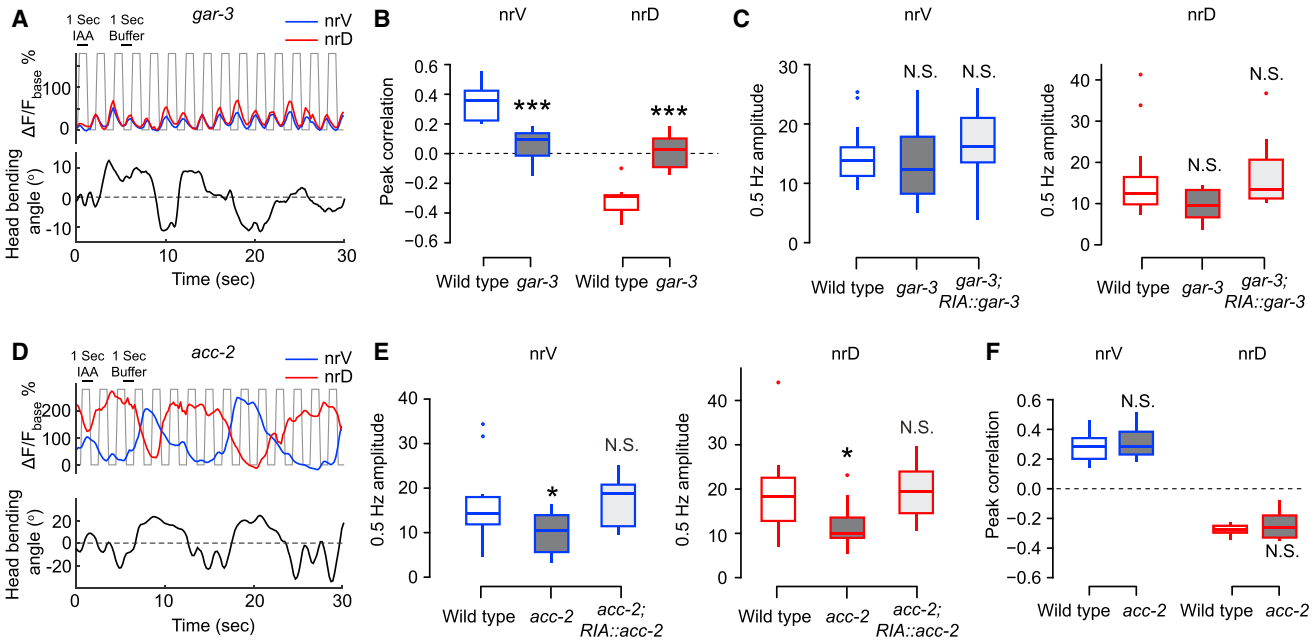

Figure 3. Cholinergic Neurotransmission Regulates the Sensory-Evoked and Motor-Encoding Activities in the RIA Axonal Domains

(A) Sample traces for the GCaMP3 signals of the nrV and the nrD axonal domains of RIA and for the head bendings in a *gar-3(gk305)* mutant animal stimulated with 0.5 Hz pulses of IAA (9.2×10^{-3} M) in a microfluidic chip. Ventral direction is positive, F_{base} is the mean intensity of the axonal signals in a few frames of low-activity state, and ΔF indicates $F - F_{base}$.

(B) When stimulated with 0.5 Hz pulses of IAA, mutating *gar-3* (n = 8 animals) significantly decreases the peak correlations between the nrV and the nrD GCaMP3 signals with the head bendings compared with wild-type (n = 8 animals).

(C) The amplitudes of the 0.5 Hz peak identified by the Fourier transform of the nrV or the nrD GCaMP3 signals are comparable in wild-type (n = 15 animals), the transgenic animals expressing a wild-type *gar-3* cDNA in the *gar-3(gk305)* mutant background (n = 10 animals), and the *gar-3* mutants (n = 9 animals) in response to 0.5 Hz IAA pulses.

(D) Sample traces for RIA axonal GCaMP5 signals and the head bendings in an *acc-2(ok2216)* mutant animal stimulated with 0.5 Hz pulses of IAA (9.2×10^{-3} M) in a microfluidic chip. Ventral direction is positive, F_{base} is the mean intensity of the axonal signals in a few frames of low-activity state, and ΔF indicates $F - F_{base}$.

(E) When stimulated with 0.5 Hz pulses of IAA, mutating *acc-2* (n = 14 animals) significantly decreases the amplitude of the 0.5 Hz peak identified by the Fourier transform of the nrV and the nrD GCaMP5 signals compared with wild-type (n = 14 animals), and the defect was rescued by expressing a wild-type *acc-2* cDNA in RIA (n = 11 animals).

(F) The *acc-2* mutation (n = 7 animals) does not alter the peak correlations between the nrV and the nrD GCaMP5 signals with the head bendings in comparison with wild-type (n = 8 animals) when stimulated with 0.5 Hz pulses of IAA.

Student's t test (B and F); one-way ANOVA (C and E). ***p < 0.001, **p < 0.01, *p < 0.05; N.S., not significant. The boxplots show the first quartile, median, and third quartile; the whiskers extend to the data points that are equal to or less than 1.5 IQR away from the first or the third quartile; dots are outliers.

See also Figure S3.

the transgenic animals that expressed a wild-type *gar-3* cDNA in RIA in the *gar-3* mutant background (Figure 3C). Thus, the muscarinic cholinergic neurotransmission mediates the motor-encoding activity of RIA axonal domains, and the two activity patterns in RIA are encoded by different signaling mechanisms.

Next, we sought the signaling that encoded the sensory-evoked synchronous activity. While both RIA and a major presynaptic interneuron, AIY, generate an in-phase response to the 0.5 Hz IAA pulses, AIY responds to the onset of IAA with increased calcium transients and RIA responds to the onset of IAA with decreased calcium transients (Figures 2A and 2F). AIY is cholinergic (Alfonso et al., 1993; Pereira et al., 2015). Thus, we sought the inhibitory cholinergic neurotransmission from AIY to RIA. The *C. elegans* genome encodes four putative acetylcholine-gated anion channels and among them only *acc-2* is expressed in RIA (Pereira et al., 2015). Previous studies show that ACC-2 functions as an acetylcholine-gated chloride channel (Putrenko et al., 2005). We found that a deletion mutation in *acc-2*, *ok2216*, disrupted the IAA-evoked synchronous response of RIA (Figure 3D), indicated by the significantly reduced amplitude of the 0.5 Hz peak identified by the Fourier transform of the GCaMP signals of nrV and nrD (Figure 3E). The defect was completely rescued by selectively expressing a wild-type cDNA of *acc-2* in RIA (Figure 3E). Meanwhile, the correlations between the head bendings and the GCaMP signals of nrV and nrD were not altered by the *acc-2* mutation (Figures 3F and S3B). Together, these results demonstrate that the chloride-mediated cholinergic neurotransmission regulates the sensory-evoked synchronous response in the RIA axonal domains.

The Sensory-Evoked Synchronous Activity Suppresses the Motor-Encoding Activity of RIA

Next, we characterized the integration of the sensory-evoked synchronous activity and the motor-encoding compartmentalized

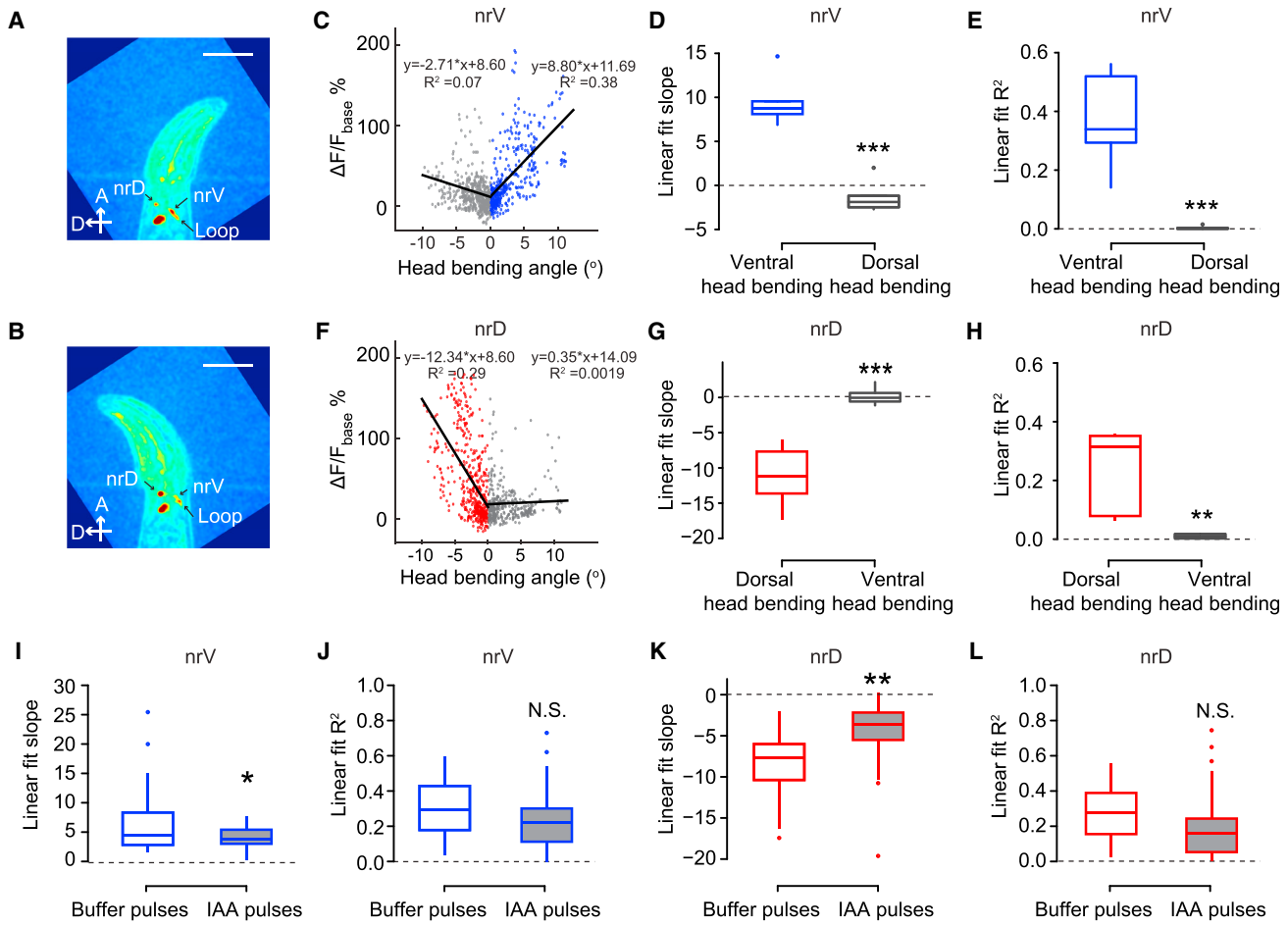

Figure 4. The Sensory-Evoked Activity of RIA Suppresses the Motor-Encoding Activity of RIA in a Microfluidic Device

(A and B) Sample frames for the GCaMP3 signals of nrV, nrD, and loop domains of RIA during a ventral head bending (A) or a dorsal head bending (B). The frames are pseudo-colored (ImageJ) to better demonstrate GCaMP3 signals. A, anterior; D, dorsal. Scale bar, 50 μm. The worm body is inside of a channel with the head outside.

(C) Sample plot showing the linear regression fit of the GCaMP3 signal of nrV in one worm as a function of the ventral or the dorsal head bending angles. Ventral direction is positive, each dot indicates the nrV GCaMP3 signal and the head bending angle in one frame, and the plot represents the results from one movie.

(D and E) Compared with the linear fit of the nrV GCaMP3 signals and the dorsal head bending angles, the linear regression fit of the nrV GCaMP3 signals and the ventral head bending angles generates steeper slopes (D) and bigger coefficients of determination (E). n = 6 animals, Student's t test.

(F) Sample plot showing the linear regression fit of the GCaMP3 signal of nrD in one worm as a function of the ventral or the dorsal head bending angles. Ventral direction is positive and each dot indicates the GCaMP3 signal of nrD and the head bending angle in one movie frame; the plot represents the results from one movie.

(G and H) Compared with the linear fit of the nrD GCaMP3 signals and the ventral head bending angles, the linear regression fit of the nrD GCaMP3 signals and the dorsal head bending angels generates steeper slopes (G) and bigger coefficients of determination (H). n = 6 animals, Student's t test.

(I–L) In comparison with the buffer pulses (n = 22 animals), IAA pulses (9.2×10^{-3} M, n = 29 animals) significantly reduce the steepness of the slopes for the linear fit of the nrV GCaMP3 signals and the ventral head bending angles (I) and for the linear fit of the nrD GCaMP3 signals and the dorsal head bending angles (K) without altering the coefficients of determination (J and L). Student's t test.

***p < 0.001, **p < 0.01, *p < 0.05; N.S., not significant. The boxplots show the first quartile, median, and third quartile; the whiskers extend to the data points that are equal to or less than 1.5 IQR away from the first or the third quartile; dots are outliers. F_{base} is the mean intensity of the axonal signals in a few frames of low-activity state; ΔF indicates $F - F_{base}$.

activity that were simultaneously present and independently encoded in RIA. We first analyzed the intensity of the motor-encoding activity and the amplitude of head bendings in the absence of olfactory stimulation in a microfluidic chip. We defined the ventral direction as positive and performed linear regression analysis between the intensity of the axonal GCaMP signals and the head bending amplitude (Figures 4A and 4B). We found that compared with the linear fit of the nrV GCaMP signals and the dorsal head bending amplitudes, the linear fit of the nrV GCaMP signals and the ventral bending amplitudes generated a steeper linear fit slope and a bigger coefficient of determination R^2 (Figures 4C–4E); conversely, compared with the linear fit of the nrD GCaMP signals and the ventral bending amplitudes, the linear fit of the nrD GCaMP signals and the dorsal bending amplitudes generated a steeper linear fit slope and a bigger coefficient of determination R^2 (Figures 4F–4H). These results indicate that the GCaMP signals of nrV and nrD encode the amplitudes of the ventral and the dorsal head bendings, respectively. Next, we stimulated the animals

with 0.5 Hz pulses of IAA or buffer. We found that compared with the buffer control, the stimulation of the IAA pulses significantly decreased the slope for the linear fit of the nrV GCaMP signals and the ventral bending amplitudes and the slope for the linear fit of the nrD GCaMP signals and the dorsal bending amplitudes without significantly altering the coefficients of determination (Figures 4I–4L). These results indicate that the sensory-evoked axonal activity of RIA suppresses the motor-encoding activity of the same axonal domains. The suppression underlies the sensorimotor integration in RIA.

The microfluidic chip allowed us to precisely control the temporal pattern of the sensory stimulation to aid the characterization of the interaction of the sensory-evoked and the motor-encoding activities in RIA. Next, we recorded the GCaMP signals in RIA in freely moving animals to investigate the function of RIA sensorimotor integration in olfactory steering (STAR Methods). We quantified the GCaMP signals in the nrV and the nrD domains of RIA, as well as the direction and the amplitude of the head undulation in each movie frame. We defined the ventral direction of head undulations as the positive direction and performed cross-correlation analysis. We found that in animals that freely moved on the surface of a standard agar plate, the GCaMP signals of nrV and nrD correlated with the amplitude of the ventral and the dorsal head undulations, respectively (Figures 5A and 5B; Movie S3). To control potential motion effects, we performed the same imaging experiments with transgenic animals that expressed both GGaMP3 and mCherry in RIA and used the signal of mCherry to normalize the signal of GCaMP3 and reached the same conclusion (Figure 5C). We also performed similar analysis on transgenic animals that selectively expressed GFP in RIA and did not detect any correlation between the GFP signal in either nrV or nrD with head undulations (Figure 5D). These results demonstrate in freely moving animals that the activity of nrV or nrD encodes the motor state of the ventral or the dorsal head undulations, respectively.

Next, we characterized the sensorimotor integration of RIA during olfactory steering. We recorded the GCaMP signal of RIA in animals that first freely moved on a standard agar plate for 1–2 min and then, after a drop of IAA was added to the plate, performed steering toward IAA (Figure 5E; STAR Methods). We quantified the GCaMP signals of nrV and nrD during each head undulation to obtain the mean values for all the head undulations in the absence of IAA and that in the presence of IAA. We compared the average GCaMP signals from multiple worms in the absence of IAA with that during steering toward IAA. We found that nrV and nrD displayed significantly lower activity during steering toward IAA than during sinusoidal movements in the absence of IAA (Figure 5F). This difference was abolished by the deletion mutation in the *eat-4(ky5)* mutant animals (Figure 5G). *eat-4* is required for the glutamatergic neurotransmission underlying the olfactory response to IAA (Chalasani et al., 2007). *eat-4* is needed for RIA to generate oscillatory sensory responses to IAA pulses (Figure 2E). Our results indicate that the sensory response in RIA suppresses the motor activity that encodes the head undulations when the worm steers toward IAA.

Next, we addressed the mechanisms underlying the sensorimotor integration in RIA during olfactory steering by examining the function of GAR-3 and ACC-2. First, we found that the RIA axonal GCaMP signals in the *gar-3(gk305)* mutant animals lost the correlation with the head undulations in freely moving animals regardless of the presence of the odorant (Figure 5H). However, the presence of IAA continued to suppress the activities of nrV and nrD in *gar-3(gk305)* (Figure 5H). The defect in *gar-3(gk305)* was rescued by selectively expressing a wild-type *gar-3* gene in RIA (Figure 5I). In contrast, the *acc-2(ok2216)* mutation completely abolished the suppressive effect of IAA on the activities of nrV and nrD during steering toward IAA (Figure 5J). Expressing a wild-type *acc-2* cDNA selectively in RIA rescued the defect in the *acc-2(ok2216)* animals (Figure 5K). These results indicate that during olfactory steering, the interaction between the *gar-3*-mediated motor-encoding activity and the *acc-2*-mediated sensory-encoding activity allows the activity of the RIA axonal domains to simultaneously represent the information of the head undulations and the odorant.

RIA Sensorimotor Integration Decodes the Spatial Information of the Odorant during Steering

Next, we asked how the sensorimotor integration in RIA regulates olfactory steering. Because the worms were able to steer toward IAA with either the ventral or the dorsal side of their bodies closer to the odorant, we asked how the worms decoded the information of the odorant location to regulate steering toward the odorant. We analyzed the activity of the nrV and the nrD RIA axonal domains in animals that steered toward the IAA drop that was located either on the ventral or the dorsal side of their bodies (Figure 6A). We found that when IAA was on the ventral side of the animal, the GCaMP signal of nrV was significantly weaker than that of nrD; conversely, when IAA was on the dorsal side of the animal, the GCaMP signal of nrD was significantly weaker than that of nrV (Figure 6B). When steering toward a ventrally located IAA source, a worm samples higher concentrations of IAA during the ventral head undulations than during the dorsal head undulations. Because the ventral head undulations are the active states of nrV and the inactive states of nrD (Figures 5A and 5B), the ventrally located IAA source generates a stronger suppression of nrV activity than nrD activity (Figure 6B). Conversely, when steering toward a dorsally located IAA source, a worm samples higher IAA concentrations during the dorsal head undulations than during the ventral head undulations. Because the dorsal head undulations are the active states of nrD and the inactive states of nrV (Figures 5A and 5B), the dorsally located IAA source generates a stronger sensory-evoked suppression of nrD activity than nrV activity (Figure 6B). As a result, sensorimotor integration in RIA produces an asymmetry between the activity of nrV and the activity of nrD during steering toward IAA. The asymmetry between the RIA axonal activities was completely abolished by the mutation *ky5* in *eat-4* (Figure 6C), which was required for the sensory-evoked synchronous response in RIA (Figure 2E). These results indicate that the integration of the activity that represents the head undulations with the activity that represents the sensory response to the odorant in the RIA axonal domains transforms the spatial information of the odorant into the asymmetry between the activities of the nrV and the nrD domains.

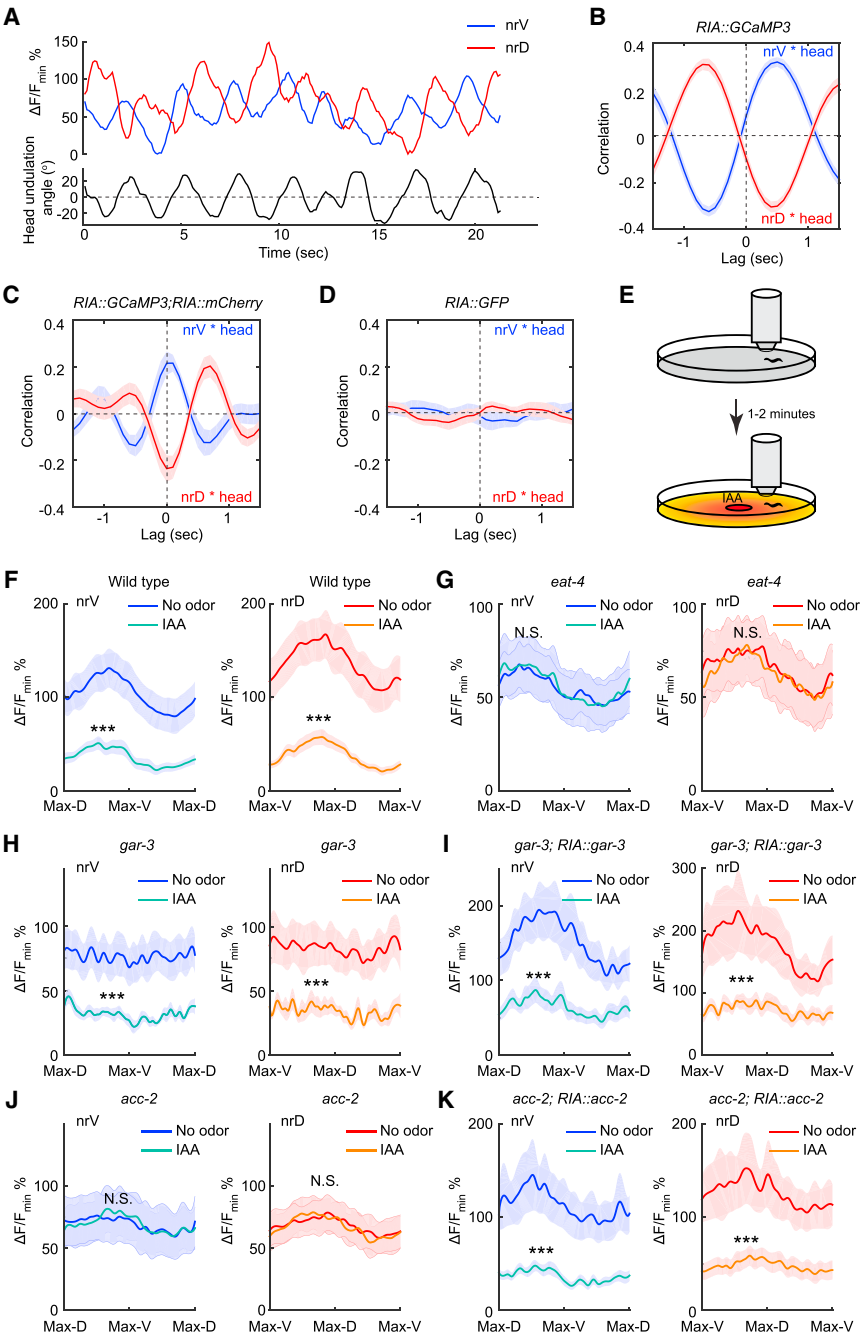

Figure 5. Cholinergic Neurotransmission Regulates Sensorimotor Integration in RIA during Olfactory Steering toward IAA

(A) Sample traces for the GCaMP3 signals of the nrV and the nrD axonal domains of RIA and the amplitudes of head undulations in a freely moving animal. Ventral direction is positive, F_{min} is the minimal intensity for the movie, and ΔF indicates $F - F_{min}$.

(B) The GCaMP3 signals of nrV and nrD correlate with the ventral and dorsal head undulations, respectively, in freely moving animals. n = 27 animals.

(C) The GCaMP3 signals of nrV and nrD normalized with the mCherry signals of the same domains correlate with the ventral and the dorsal head undulations, respectively, in freely moving animals. n = 28 animals.

(D) The GFP signals of nrV and nrD do not correlate with the head undulations in freely moving animals. n = 9 animals.

In (B)–(D), ventral direction is positive, solid lines represent mean, and shades represent SEM.

(E) Schematics showing the procedure of *in vivo* calcium imaging in freely moving animals first in the absence of any odorant and then in the presence of IAA.

(F) The GCaMP3 signals of nrV and nrD are significantly smaller during olfactory steering toward a drop of IAA (9.2×10^{-3} M) than during freely moving in the absence of an odorant. n = 33 animals.

(G) The sensory-evoked suppression of the GCaMP3 signals in the RIA axonal domains in steering animals is abolished in *eat-4(ky5)* mutants. n = 22 animals.

(H and I) Mutating *gar-3* abolishes the correlation of the RIA axonal GCaMP3 signals with the head undulations while maintaining the sensory-evoked suppression of the axonal activity (H; n = 17 animals); expressing a wild-type *gar-3* cDNA selectively in RIA rescues the defect (I; n = 25 animals).

(J and K) Mutating *acc-2* abolishes the sensory-evoked suppression of the RIA axonal GCaMP5 signals (J; n = 24 animals); expressing a wild-type *acc-2* cDNA selectively in RIA rescues the defect (K; n = 26 animals).

In (F)–(K), F_{min} is the minimal intensity of GCaMP3 or GCaMP5 signals for each worm; ΔF indicates $F - F_{min}$. The GCaMP signals of nrV and nrD over each complete head undulation (for nrV, from the maximal dorsal [Max-D] position to the maximal ventral [Max-V] positon and back to the maximal dorsal [Max-D] position; for nrD, from the maximal ventral [Max-V] position to the maximal dorsal [Max-D] positon and back to the maximal ventral [Max-V] position) are measured and the averages for all the head undulations made by each worm are generated, which are used to generate mean and SEM, represented by solid lines and shades, respectively, for multiple worms. Kolmogorov-Smirnov test (MATLAB) is used to compare the mean values, ***$p < 0.001$; N.S., not significant.

See also Figure S4 and Movie S3.

The Asymmetry in the RIA Axonal Activities Curves the Locomotory Trajectory

To characterize how the asymmetry in the RIA axonal activities, measured by the intensity of GCaMP signals, regulates steering, we examined the behavioral effect of the synaptic release of the RIA axonal domains, because intracellular calcium stimulates synaptic release (Südhof, 2013). The nrV and the nrD axonal domains of RIA send synapses to a group of head motor neurons, including the SMD motor neurons that innervate the dorsal and the ventral head muscles and control the amplitude of the dorsal-ventral head undulations during sinusoidal movements (Gray et al., 2005; Shen et al., 2016; White et al., 1986; Figure 1D).

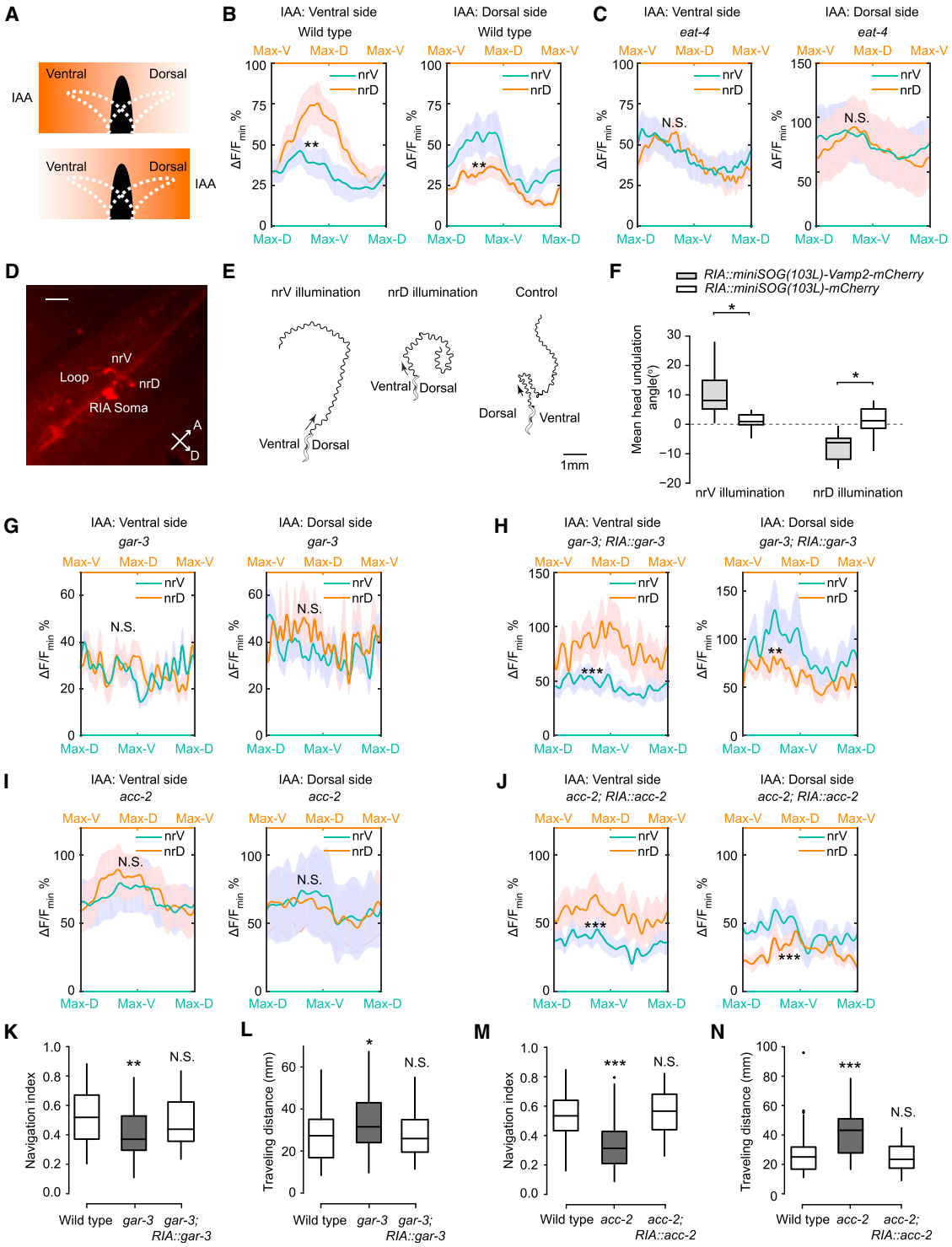

Figure 6. The Cholinergic Sensorimotor Integration in RIA Decodes the Spatial Information of the Odorant to Bias the Steering Trajectory

(A) Schematics showing the sampling head movements when a worm steers toward isoamyl alcohol (IAA) located on the ventral or the dorsal side of the animal.

(B) The GCaMP3 signal of nrV is significantly weaker than that of nrD when animals steer toward IAA located on the ventral side of the animals (n = 18 animals), and the GCaMP3 signal of nrD is significantly weaker than that of nrV when animals steer toward IAA located on the dorsal side (n = 15 animals).

(C) The mutation in *eat-4(ky5)* abolishes the asymmetry between the RIA axonal GCaMP3 signals during steering toward IAA regardless of the location of IAA. n = 11 animals each condition.

(legend continued on next page)

We generated a chimeric protein by fusing the vesicle-associated membrane protein synaptobrevin 2/VAMP2 with an isoform of miniSOG. When illuminated with a blue light, miniSOG generates a singlet reactive oxygen species that inactivates proteins in the proximity (Shu et al., 2011). Expressing VAMP2-miniSOG in the mammalian or the *C. elegans* neurons inhibits synaptic release by disrupting the function of synaptic vesicles (Lin et al., 2013). We used a more efficient isoform of miniSOG, Q103L (Xu and Chisholm, 2016), and selectively expressed VAMP2-miniSOG(103L) in RIA. We found that the fusion protein was in the soma and the axon (Figure 6D). To selectively block the synaptic release from nrV or nrD, we focused the blue light illumination on either one of the two domains and quantified the average angle of the head undulations during sinusoidal movements in the operated animals (STAR Methods). We found that selectively blocking the synaptic release of nrV produced head undulations that were biased toward the ventral side of the operated worms and generated trajectories that curved toward the ventral direction; conversely, selectively blocking the synaptic release of nrD produced head undulations that were biased toward the dorsal side of the operated worms and generated trajectories that curved toward the dorsal direction. In contrast, the control animals that expressed an untagged miniSOG(103L) in RIA and went through the same handling showed no detectable bias in the dorsal or the ventral direction (Figures 6E and 6F). Together, our results indicate that the weaker activity of nrV compared to nrD, resulting from integrating the information of ventrally located IAA and the state of the head undulations, generates the biases toward the ventral direction in the locomotory trajectories, and that the weaker activity of nrD compared to nrV, resulting from integrating the information of dorsally located IAA and the state of the head undulations, generates the biases toward the dorsal direction in the locomotory trajectories. Thus, the sensorimotor integration in RIA directs the steering toward the odorant.

The Cholinergic Sensorimotor Integration in RIA Regulates Olfactory Steering

Next, to examine the role of cholinergic neurotransmission in regulating olfactory steering, we analyzed the asymmetry between the activities of the nrV and the nrD RIA axonal domains in the *gar-3(gk305)* and the *acc-2(ok2216)* mutant animals during steering toward IAA. We found that in *gar-3(gk305)*, although both of the RIA axonal domains showed the IAA-evoked suppression of activity (Figure 5H), the asymmetry between the axonal activities was completely abolished (Figure 6G). The defect was rescued with the selective expression of a wild-type *gar-3* cDNA in RIA (Figure 6H). These results indicate that the asymmetry in the RIA axonal activities depends on the *gar-3*-mediated neurotransmission that represents the head undulations. Conversely, in *acc-2(ok2216)*, because neither nrV nor nrD showed IAA-evoked suppression of the activity (Figure 5J), they did not exhibit any asymmetry between their activities (Figure 6I) during olfactory steering. Expressing a wild-type *acc-2* cDNA selectively in RIA restored the IAA-induced asymmetry between the activities of nrV and nrD (Figure 6J). These results indicate that the sensory-evoked asymmetry in the RIA axonal domains during olfactory steering also requires the *acc-2*-mediated neurotransmission that regulates the sensory response. At the behavioral level, in comparison with wild-type, both the *gar-3(gk305)* and the *acc-2(ok2216)* mutant animals exhibited a significantly smaller navigation index (Figures 6K and 6M) and traveled a longer distance (Figures 6L and 6N) when steering toward IAA. These defects were fully rescued by expressing a wild-type

(D) A sample image of an RIA neuron expressing miniSOG(103L)-VAMP2-mCherry. RIA soma and the axonal domains are denoted. A, anterior; D, dorsal. Scale bar, 10 μm.

(E) Sample locomotory traces generated by animals in which the synaptic release of the nrV or the nrD domain of RIA is selectively blocked with a blue-light illumination of a miniSOG(103L)-VAMP2-mCherry fusion protein expressed in RIA and a sample trace of a control animal that expresses miniSOG(103L)-mCherry in RIA. Ventral or dorsal side of the animal is denoted and arrows denote movement directions.

(F) Mean angle of the head undulations generated by animals in which the synaptic release of nrV (n = 10 and 7 animals for experiment and control, respectively) or nrD (n = 7 and 6 animals for experiment and control, respectively) domain of RIA is selectively blocked. Ventral direction is positive. Student's t test, $^{*}p < 0.05$. The boxplots show the first quartile, median, and third quartile; the whiskers extend to the data points that are equal to or less than 1.5 IQR away from the first or the third quartile; dots are outliers.

(G and H) Mutating *gar-3* abolishes the asymmetry between the GCaMP3 signals of nrV and nrD during olfactory steering toward IAA regardless of the location of IAA (G; n = 9 animals IAA on ventral side; n = 8 animals IAA on dorsal side), and expressing a wild-type *gar-3* cDNA selectively in RIA rescues the defect (H; n = 14 animals IAA on ventral side; n = 11 animals IAA on dorsal side).

(I and J) Mutating *acc-2* abolishes the asymmetry between the GCaMP5 signals of nrV and nrD during olfactory steering toward IAA regardless of the location of IAA (I; n = 13 animals IAA on ventral side; n = 11 animals IAA on dorsal side), and the defect is rescued by expressing a wild-type *acc-2* cDNA selectively in RIA (J; n = 15 animals IAA on ventral side; n = 11 animals IAA on dorsal side).

In (B), (C), and (G)–(J), F_{min} is the minimal intensity of GCaMP3 or GCaMP5 for each worm; ΔF indicates $F - F_{min}$. The GCaMP signals of nrV and nrD over each complete head undulation (for nrV, from the maximal dorsal position to the maximal ventral positon and back to the maximal dorsal position; for nrD, from the maximal ventral position to the maximal dorsal positon and back to the maximal ventral position) are measured and the averages for all the head undulations made by each worm are generated, which are used to generate mean and SEM, represented by solid lines and shades, respectively, for multiple worms. Kolmogorov-Smirnov test (MATLAB) is used to compare the mean values, $^{***}p < 0.001$, $^{**}p < 0.01$; N.S., not significant.

(K–N) The navigation index for *gar-3(gk305)* (K) or *acc-2(ok2216)* (M) mutants is significantly smaller than that for wild-type when steering toward IAA, and the defects are rescued by expressing a wild-type *gar-3* cDNA or a wild-type *acc-2* cDNA selectively in RIA in the respective mutant animals (K and M); meanwhile, the distance traveled by *gar-3(gk305)* animals (L) or *acc-2(ok2216)* animals (N) before reaching IAA is significantly longer than wild-type, and the defects are rescued by expressing a wild-type *gar-3* cDNA or a wild-type *acc-2* cDNA selectively in RIA in the respective mutant animals (L and N). n = 61 (wild-type), 59 (*gar-3* mutant), and 40 (*gar-3; RIA::gar-3* transgenic) animals (K and L); n = 35 (wild-type), 43 (*acc-2* mutant), and 41 (*acc-2; RIA::acc-2* transgenic) animals (M and N). One-way ANOVA, $^{***}p < 0.001$, $^{**}p < 0.01$, $^{*}p < 0.05$; N.S., not significant. The boxplots show the first quartile, median, and third quartile; the whiskers extend to the data points that are equal to or less than 1.5 IQR away from the first or the third quartile; dots are outliers.

See also Figure S4.

gar-3 cDNA or a wild-type *acc-2* cDNA selectively in RIA in the respective mutant animals (Figures 6K–6N). Together, our results show that two different types of cholinergic neurotransmission independently encode the sensory response and the motor state of the animal in the axon of RIA and that the integration of these two signals transforms the spatial information of the attractive odorant into the asymmetry between the activities of the RIA axonal domains, resulting in the biased locomotory trajectory toward the odorant (Figure S4).

Aversive Olfactory Training Modulates RIA Sensorimotor Integration and Olfactory Steering

Our previous studies show that *C. elegans* learns to reduce its preference to the smell of pathogenic bacteria, such as the *Pseudomonas aeruginosa* strain PA14, after feeding on the pathogen for a few hours at the adult stage. This form of aversive learning depends on a serotonin signal, which is demonstrated by the loss of learning in mutants defective in serotonin production, and the function of the interneuron RIA is required to generate the learned preference (Ha et al., 2010; Jin et al., 2016; Zhang et al., 2005; Figure S5). We quantified the GCaMP signal of the RIA axonal domains in naive animals that were cultivated under the standard condition and the animals that were trained with PA14 for 6 hr during the adult stage. We stimulated the animals with 0.5 Hz pulses of the supernatant of an overnight culture of PA14 or OP50. We found that the nrV and the nrD axonal domains in the naive and the trained animals generated synchronous responses to the oscillatory stimulations of PA14 or OP50 (Figures 7A–7D). The average GCaMP signals in the RIA axonal domains were weaker in the trained animals than in the naive animals in response to both PA14 and OP50; however, the amplitude of the 0.5 Hz peak identified by the Fourier transform of the GCaMP signals of nrV and nrD was significantly smaller in the trained animals than in the naive animals only when the animals were stimulated with the supernatant of PA14 culture (Figures 7A–7F). The amplitudes of the 0.5 Hz peak in the Fourier transforms of the axonal GCaMP signals evoked by 0.5 Hz pulses of the culture supernatant of the *E. coli* strain OP50, the standard food for the worm, were comparable in the naive and the trained animals (Figures 7C–7F). These results demonstrate that aversive training with PA14 modulates the sensory-evoked synchronous response of RIA in a way that is specific to the training experience.

Our findings together predict that a decreased sensory response of RIA to PA14 in trained animals, represented by a decreased amplitude of the 0.5 Hz peak identified by the Fourier transform of the axonal GCaMP signals, would weaken the asymmetry in the axonal activities and, thus, result in a reduced bias in the steering trajectory toward PA14. We found that when steering toward a drop of the supernatant from a PA14 culture, the PA14-trained animals displayed a reduced navigation index and traveled a longer distance before reaching PA14 compared with naive animals (Figures 7G and 7H). In contrast, the PA14-trained animals steered toward OP50 similarly to the naive animals (Figures 7I and 7J). Together, these results demonstrate that the sensorimotor integration in the RIA axonal domains is a dynamic process that can be modulated by experience or context to generate specific changes in the steering movements.

DISCUSSION

C. elegans Performs Sensorimotor Integration to Regulate Olfactory Steering

During goal-directed locomotion, many animals probe the environment with sampling movements, during which interaction between the sensory and motor systems directs the locomotion toward the cue. *C. elegans* moves forward on a solid substrate by making undulatory body movements on the dorsal-ventral plane (Wen et al., 2012). With the undulatory movements, one behavioral strategy that *C. elegans* uses to approach attractive odorants and salts is to steer toward the chemicals by making a curved trajectory (Albrecht and Bargmann, 2011; Iino and Yoshida, 2009; Izquierdo and Lockery, 2010; Pierce-Shimomura et al., 1999). During steering, the oscillatory body movement allows the head of the worm, and the sensory neurons located in the head, to sample the space spanned by the head undulations. This form of active sensing leads to an oscillation in the concentration of the odorant sampled by the worm (Kato et al., 2014). Here, we show that *C. elegans* performs sensorimotor integration to regulate steering toward attractive odorants. The sensorimotor integration is achieved by the suppression of the motor-encoding activity of the axonal domains of the interneuron RIA by the sensory-encoding activity of the same domains. The motor activity derives from the motor system that regulates head undulations and represents the amplitude and the dorsal-ventral direction of the head undulations, while the sensory-evoked activity represents the response to the odorant. Thus, by integrating these two types of activities RIA signals whether the odorant is on the ventral side or the dorsal side of the animal, which is represented by a stronger sensory-evoked suppression of the axonal activities during the ventral or the dorsal head undulations, respectively. As a consequence, the nrV domain displays a weaker activity than nrD when a worm steers toward ventrally located IAA and the nrD domain displays a weaker activity than nrV when a worm steers toward dorsally located IAA. Disrupting either the sensory or the motor component of the RIA axonal activity disrupts the sensorimotor integration and weakens the steering performance. We further demonstrate that the asymmetry between the synaptic outputs of the nrV and the nrD domains, which can be generated by the asymmetry between the activities of these two domains, biases the locomotory trajectory in such way that the undulatory movements bias toward the ventral side when nrV activity is weaker and the undulatory movements bias toward the dorsal side when nrD activity is weaker (Figure S4). Thus, our results uncover, at the molecular, neuronal, circuit, and behavioral levels, how the sensory and the motor signals interact to decode the information of the sensory cue and to modulate the ongoing movements in order to reach a sensory-defined goal.

Cholinergic Neurotransmission Encodes Sensory and Motor Information to Regulate Sensorimotor Integration

The connectome of the *C. elegans* nervous system (White et al., 1986) allows us to identify the sensory neural circuit that responds to rapid olfactory stimulations and transmits the sensory information to the site of integration through an acetylcholine-gated chloride channel. Meanwhile, a muscarinic acetylcholine receptor acts in the central integrating site to receive the

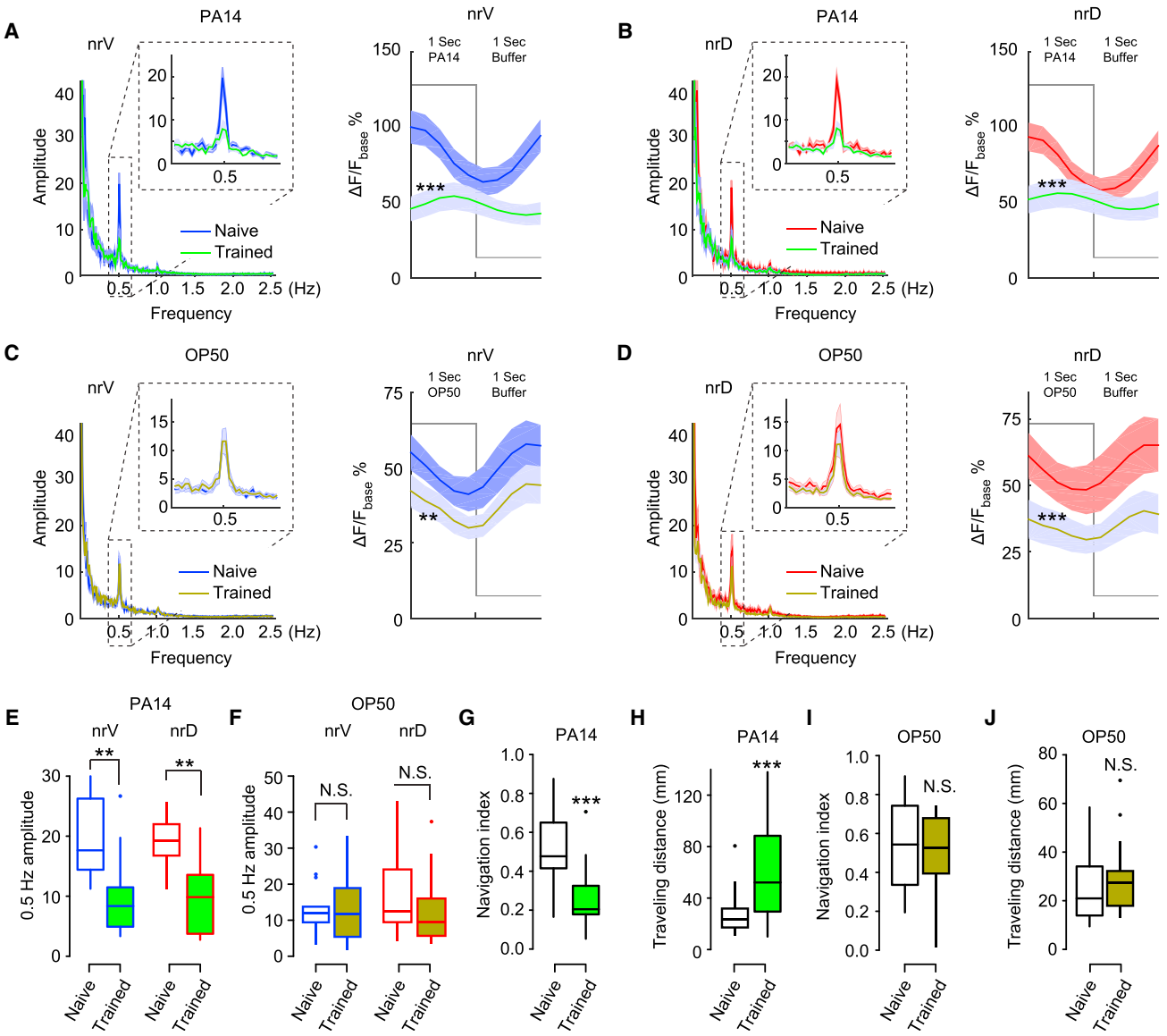

Figure 7. Aversive Olfactory Training Modulates Sensorimotor Integration in RIA to Generate Experience-Specific Changes in Olfactory Steering

(A–D) When stimulated with 0.5 Hz pulses of the supernatant of the culture of *P. aeruginosa* PA14, animals trained with PA14 display a decreased amplitude in the 0.5 Hz peak identified by the Fourier transform of the GCaMP3 signals and decreased average GCaMP3 signals per stimulation cycle of the nrV (A) and the nrD (B) axonal domains of RIA (A and B; n = 9 naive animals, n = 11 trained animals); however, when stimulated with 0.5 Hz pulses of the supernatant of *E. coli* OP50, animals trained with PA14 display only decreased average axonal GCaMP3 signals per stimulation cycle without altering the amplitude of the 0.5 Hz peak identified by the Fourier transform of the GCaMP3 signals (C and D; n = 13 naive animals, n = 15 trained animals). Left panels show the average traces of the Fourier transforms of the GCaMP3 signals of multiple worms and the right panels show the average GCaMP3 signals per stimulation cycle of multiple worms. n, number of worms. Solid lines represent mean; shades represent SEM. F_{base} is the mean intensity of the axonal signals in a few frames of low-activity state; ΔF indicates $F - F_{base}$. Kolmogorov-Smirnov test (MATLAB) is used to compare the mean values of $\Delta F/F_{base}$ %, ***$p < 0.001$, **$p < 0.01$.

(E and F) Quantitation of the amplitudes of the 0.5 Hz peaks identified by the Fourier transform of the RIA axonal GCaMP3 signals shown in (A) and (B) (E; n = 9 naive animals, n = 11 trained animals) and (C) and (D) (F; n = 13 naive animals, n = 15 trained animals).

(G–J) Animals trained with PA14 display a decreased navigation index (G) and a longer traveling distance (H) when steering toward the supernatant of PA14 in comparison with naive animals (G and H; n = 29 naive animals, n = 25 trained animals), but display a navigation index (I) and a traveling distance (J) that are similar to those in naive animals when steering toward the supernatant of OP50 (I and J; n = 41 naive animals, n = 46 trained animals).

In (E)–(J), Student's t test, ***$p < 0.001$, **$p < 0.01$; N.S., not significant. The boxplots show the first quartile, median, and third quartile; the whiskers extend to the data points that are equal to or less than 1.5 IQR away from the first or the third quartile; dots are outliers.

See also Figure S5.

information of head undulations from the motor system. We further show that the integrating axonal domains send synaptic outputs to bias the ongoing head undulations. Thus, using a system that is dissectible at the level of neural circuits and the underlying molecular machinery, our study reveals a compact cholinergic network that integrates the ongoing motor state with sensory processing to mediate behavioral decisions during active exploration. These findings expand our understanding of the diverse function of the cholinergic signals in the nervous systems that have evolved through different pathways. For example, in the mammalian central nervous system, the basal forebrain cholinergic terminals in the prefrontal cortex can respond to sensory cues (Howe et al., 2013; Parikh et al., 2007), while the basal forebrain cholinergic inputs to various sensory cortices are able to carry motor information (Eggermann et al., 2014; Fu et al., 2014; Lee et al., 2014; Nelson and Mooney, 2016). We speculate that the wide range of the brain regions innervated by the central cholinergic system and various temporal dynamics of the cholinergic signals enabled by multiple acetylcholine-gated channels and receptors subserve the function of the cholinergic system in encoding different types of sensory and motor information.

Sensorimotor Integration Generates Adaptive Behavioral Outputs under Various Contexts

The mature nervous system has a remarkable ability to generate behavioral outputs of adaptive values under different contexts. How the developed and hardwired neural network simultaneously encodes different behavioral outputs is not fully understood. Previous studies characterize a form of olfactory learning in *C. elegans* in which the worm learns to reduce the preference to the smell of a pathogenic bacterium after feeding on the pathogen for a few hours. The RIA interneuron plays a critical role in the learning paradigms (Ha et al., 2010; Jin et al., 2016). Here, we demonstrate the function of RIA during olfactory steering in both naive and learned adult animals. We find that naive animals without RIA synaptic outputs steer toward a point source of an attractive odorant with a significantly reduced efficiency. During steering, RIA integrates the sensory information, which is collected through active sampling movements, with the motor state of the head undulations to modulate the ongoing locomotion. Meanwhile, the finding that animals without RIA synaptic outputs are still able to reach the odorant is consistent with the presence of an independent sensorimotor circuit in the wiring diagram of the worm and is consistent with previous studies that characterize different behavioral strategies for *C. elegans* chemotaxis (Albrecht and Bargmann, 2011; Hums et al., 2016; Iino and Yoshida, 2009; Pierce-Shimomura et al., 1999). In addition, we show that RIA displays an experience-dependent change in the sensory response to the training bacteria. We propose that the change occurs upstream of RIA because the sensory response of RIA to the benign bacteria is not similarly altered in the trained animals. Interestingly, the experience-dependent changes in the adult-trained animals (Figure 7) differ from that in animals trained during the first larval stage (Jin et al., 2016), suggesting that the activity of RIA can be modulated differently. Thus, our findings show that through sensorimotor integration RIA transforms the changes in the sensory response into experience-dependent changes in the steering movements toward the training bacteria. Together, our results reveal sensorimotor integration as a neuronal and circuit mechanism underlying the interaction between the sensory and motor systems to regulate ongoing movements under various contexts.

STAR★METHODS

Detailed methods are provided in the online version of this paper and include the following:

- KEY RESOURCES TABLE
- CONTACT FOR REAGENT AND RESOURCE SHARING
- EXPERIMENTAL MODEL AND SUBJECT DETAILS
- METHOD DETAILS
  - Transgenes and transgenic animals
  - Calcium imaging
  - Olfactory steering
  - Light-induced inactivation with miniSOG
  - Aversive olfactory training and learning assay
- QUANTIFICATION AND STATISTICAL ANALYSIS
- DATA AND SOFTWARE AVAILABILITY

SUPPLEMENTAL INFORMATION

Supplemental Information includes five figures, three movies, and supplemental methods and can be found with this article online at https://doi.org/10.1016/j.neuron.2017.12.003.

ACKNOWLEDGMENTS

We thank *Caenorhabditis Genetics Center*, which is funded by the NIH Office of Research Infrastructure Programs (P40 OD010440), for strains. We thank Alejandro Lopez-Cruz in the Bargmann lab for sharing his findings on the rapid odorant response of RIA. We thank Dr. Bargmann for discussion on behavioral and imaging analysis. We thank Joel Greenwood for technical support and the Zhang laboratory members for discussion on the manuscript. Y.Z. is funded by the NIH.

AUTHOR CONTRIBUTIONS

H.L. and Y.Z. designed experiments, interpreted results, and wrote the paper. H.L., W.Y., T.W., F.D., E.S., and X.J. conducted experiments and analyzed data.

DECLARATION OF INTERESTS

The authors declare no competing interests.

Received: August 29, 2017
Revised: November 6, 2017
Accepted: December 1, 2017
Published: December 28, 2017

REFERENCES

Albrecht, D.R., and Bargmann, C.I. (2011). High-content behavioral analysis of Caenorhabditis elegans in precise spatiotemporal chemical environments. Nat. Methods *8*, 599–605.

Alfonso, A., Grundahl, K., Duerr, J.S., Han, H.P., and Rand, J.B. (1993). The Caenorhabditis elegans unc-17 gene: a putative vesicular acetylcholine transporter. Science *261*, 617–619.

Ballinger, E.C., Ananth, M., Talmage, D.A., and Role, L.W. (2016). Basal forebrain cholinergic circuits and signaling in cognition and cognitive decline. Neuron *91*, 1199–1218.

Bargmann, C.I., and Horvitz, H.R. (1991). Chemosensory neurons with overlapping functions direct chemotaxis to multiple chemicals in C. elegans. Neuron *7*, 729–742.

Bargmann, C.I., Hartwieg, E., and Horvitz, H.R. (1993). Odorant-selective genes and neurons mediate olfaction in C. elegans. Cell *74*, 515–527.

Beverly, M., Anbil, S., and Sengupta, P. (2011). Degeneracy and neuromodulation among thermosensory neurons contribute to robust thermosensory behaviors in Caenorhabditis elegans. J. Neurosci. *31*, 11718–11727.

Brenner, S. (1974). The genetics of Caenorhabditis elegans. Genetics *77*, 71–94.

Brockie, P.J., Madsen, D.M., Zheng, Y., Mellem, J., and Maricq, A.V. (2001). Differential expression of glutamate receptor subunits in the nervous system of Caenorhabditis elegans and their regulation by the homeodomain protein UNC-42. J. Neurosci. *21*, 1510–1522.

Chalasani, S.H., Chronis, N., Tsunozaki, M., Gray, J.M., Ramot, D., Goodman, M.B., and Bargmann, C.I. (2007). Dissecting a circuit for olfactory behaviour in Caenorhabditis elegans. Nature *450*, 63–70.

Chronis, N., Zimmer, M., and Bargmann, C.I. (2007). Microfluidics for in vivo imaging of neuronal and behavioral activity in Caenorhabditis elegans. Nat. Methods *4*, 727–731.

Eggermann, E., Kremer, Y., Crochet, S., and Petersen, C.C. (2014). Cholinergic signals in mouse barrel cortex during active whisker sensing. Cell Rep. *9*, 1654–1660.

Fu, Y., Tucciarone, J.M., Espinosa, J.S., Sheng, N., Darcy, D.P., Nicoll, R.A., Huang, Z.J., and Stryker, M.P. (2014). A cortical circuit for gain control by behavioral state. Cell *156*, 1139–1152.

Gordus, A., Pokala, N., Levy, S., Flavell, S.W., and Bargmann, C.I. (2015). Feedback from network states generates variability in a probabilistic olfactory circuit. Cell *161*, 215–227.

Gray, J.M., Hill, J.J., and Bargmann, C.I. (2005). A circuit for navigation in Caenorhabditis elegans. Proc. Natl. Acad. Sci. USA *102*, 3184–3191.

Ha, H.I., Hendricks, M., Shen, Y., Gabel, C.V., Fang-Yen, C., Qin, Y., Colón-Ramos, D., Shen, K., Samuel, A.D., and Zhang, Y. (2010). Functional organization of a neural network for aversive olfactory learning in Caenorhabditis elegans. Neuron *68*, 1173–1186.

Hasselmo, M.E., and Sarter, M. (2011). Modes and models of forebrain cholinergic neuromodulation of cognition. Neuropsychopharmacology *36*, 52–73.

Hendricks, M., and Zhang, Y. (2013). Complex RIA calcium dynamics and its function in navigational behavior. Worm *2*, e25546.

Hendricks, M., Ha, H., Maffey, N., and Zhang, Y. (2012). Compartmentalized calcium dynamics in a C. elegans interneuron encode head movement. Nature *487*, 99–103.

Hobert, O., Mori, I., Yamashita, Y., Honda, H., Ohshima, Y., Liu, Y., and Ruvkun, G. (1997). Regulation of interneuron function in the C. elegans thermoregulatory pathway by the ttx-3 LIM homeobox gene. Neuron *19*, 345–357.

Howe, W.M., Berry, A.S., Francois, J., Gilmour, G., Carp, J.M., Tricklebank, M., Lustig, C., and Sarter, M. (2013). Prefrontal cholinergic mechanisms instigating shifts from monitoring for cues to cue-guided performance: converging electrochemical and fMRI evidence from rats and humans. J. Neurosci. *33*, 8742–8752.

Hums, I., Riedl, J., Mende, F., Kato, S., Kaplan, H.S., Latham, R., Sonntag, M., Traunmüller, L., and Zimmer, M. (2016). Regulation of two motor patterns enables the gradual adjustment of locomotion strategy in Caenorhabditis elegans. eLife *5*, e14116.

Iino, Y., and Yoshida, K. (2009). Parallel use of two behavioral mechanisms for chemotaxis in Caenorhabditis elegans. J. Neurosci. *29*, 5370–5380.

Izquierdo, E.J., and Lockery, S.R. (2010). Evolution and analysis of minimal neural circuits for klinotaxis in Caenorhabditis elegans. J. Neurosci. *30*, 12908–12917.

Jin, X., Pokala, N., and Bargmann, C.I. (2016). Distinct circuits for the formation and retrieval of an imprinted olfactory memory. Cell *164*, 632–643.

Karpov, A. (1980). Analysis of neuron activity in the rabbit's olfactory bulb during food-acquisition behavior. In Neural Mechanisms of Goal-Directed Behavior, R. Thompson, L. Hicks, and V.B. Shvyrkov, eds. (Academic Press), pp. 273–282.

Kato, S., Xu, Y., Cho, C.E., Abbott, L.F., and Bargmann, C.I. (2014). Temporal responses of C. elegans chemosensory neurons are preserved in behavioral dynamics. Neuron *81*, 616–628.

Kato, S., Kaplan, H.S., Schrödel, T., Skora, S., Lindsay, T.H., Yemini, E., Lockery, S., and Zimmer, M. (2015). Global brain dynamics embed the motor command sequence of Caenorhabditis elegans. Cell *163*, 656–669.

Kepecs, A., Uchida, N., and Mainen, Z.F. (2006). The sniff as a unit of olfactory processing. Chem. Senses *31*, 167–179.

Kim, D.H., Feinbaum, R., Alloing, G., Emerson, F.E., Garsin, D.A., Inoue, H., Tanaka-Hino, M., Hisamoto, N., Matsumoto, K., Tan, M.W., and Ausubel, F.M. (2002). A conserved p38 MAP kinase pathway in Caenorhabditis elegans innate immunity. Science *297*, 623–626.

Laing, D.G. (1986). Identification of single dissimilar odors is achieved by humans with a single sniff. Physiol. Behav. *37*, 163–170.

Lee, D., Jung, S., Ryu, J., Ahnn, J., and Ha, I. (2008). Human vesicular glutamate transporters functionally complement EAT-4 in C. elegans. Mol. Cells *25*, 50–54.

Lee, A.M., Hoy, J.L., Bonci, A., Wilbrecht, L., Stryker, M.P., and Niell, C.M. (2014). Identification of a brainstem circuit regulating visual cortical state in parallel with locomotion. Neuron *83*, 455–466.

Lin, J.Y., Sann, S.B., Zhou, K., Nabavi, S., Proulx, C.D., Malinow, R., Jin, Y., and Tsien, R.Y. (2013). Optogenetic inhibition of synaptic release with chromophore-assisted light inactivation (CALI). Neuron *79*, 241–253.

Luo, L., Wen, Q., Ren, J., Hendricks, M., Gershow, M., Qin, Y., Greenwood, J., Soucy, E.R., Klein, M., Smith-Parker, H.K., et al. (2014). Dynamic encoding of perception, memory, and movement in a C. elegans chemotaxis circuit. Neuron *82*, 1115–1128.

MacIver, M.A., Sharabash, N.M., and Nelson, M.E. (2001). Prey-capture behavior in gymnotid electric fish: motion analysis and effects of water conductivity. J. Exp. Biol. *204*, 543–557.

Mello, C.C., Kramer, J.M., Stinchcomb, D., and Ambros, V. (1991). Efficient gene transfer in C.elegans: extrachromosomal maintenance and integration of transforming sequences. EMBO J. *10*, 3959–3970.

Nelson, A., and Mooney, R. (2016). The basal forebrain and motor cortex provide convergent yet distinct movement-related inputs to the auditory cortex. Neuron *90*, 635–648.

Nguyen, J.P., Shipley, F.B., Linder, A.N., Plummer, G.S., Liu, M., Setru, S.U., Shaevitz, J.W., and Leifer, A.M. (2016). Whole-brain calcium imaging with cellular resolution in freely behaving Caenorhabditis elegans. Proc. Natl. Acad. Sci. USA *113*, E1074–E1081.

Parikh, V., Kozak, R., Martinez, V., and Sarter, M. (2007). Prefrontal acetylcholine release controls cue detection on multiple timescales. Neuron *56*, 141–154.

Park, Y.S., Kim, S., Shin, Y., Choi, B., and Cho, N.J. (2003). Alternative splicing of the muscarinic acetylcholine receptor GAR-3 in Caenorhabditis elegans. Biochem. Biophys. Res. Commun. *308*, 961–965.

Pereira, L., Kratsios, P., Serrano-Saiz, E., Sheftel, H., Mayo, A.E., Hall, D.H., White, J.G., LeBoeuf, B., Garcia, L.R., Alon, U., and Hobert, O. (2015). A cellular and regulatory map of the cholinergic nervous system of C. elegans. eLife *4*, e12432.

Pierce-Shimomura, J.T., Morse, T.M., and Lockery, S.R. (1999). The fundamental role of pirouettes in Caenorhabditis elegans chemotaxis. J. Neurosci. *19*, 9557–9569.

Putrenko, I., Zakikhani, M., and Dent, J.A. (2005). A family of acetylcholine-gated chloride channel subunits in Caenorhabditis elegans. J. Biol. Chem. *280*, 6392–6398.

Schiavo, G., Benfenati, F., Poulain, B., Rossetto, O., Polverino de Laureto, P., DasGupta, B.R., and Montecucco, C. (1992). Tetanus and botulinum-B neurotoxins block neurotransmitter release by proteolytic cleavage of synaptobrevin. Nature *359*, 832–835.

Shen, Y., Wen, Q., Liu, H., Zhong, C., Qin, Y., Harris, G., Kawano, T., Wu, M., Xu, T., Samuel, A.D., and Zhang, Y. (2016). An extrasynaptic GABAergic signal modulates a pattern of forward movement in Caenorhabditis elegans. eLife *5*, e14197.

Shu, X., Lev-Ram, V., Deerinck, T.J., Qi, Y., Ramko, E.B., Davidson, M.W., Jin, Y., Ellisman, M.H., and Tsien, R.Y. (2011). A genetically encoded tag for correlated light and electron microscopy of intact cells, tissues, and organisms. PLoS Biol. *9*, e1001041.

Srinivasan, M.V. (2011). Honeybees as a model for the study of visually guided flight, navigation, and biologically inspired robotics. Physiol. Rev. *91*, 413–460.

Südhof, T.C. (2013). Neurotransmitter release: the last millisecond in the life of a synaptic vesicle. Neuron *80*, 675–690.

Venkatachalam, V., Ji, N., Wang, X., Clark, C., Mitchell, J.K., Klein, M., Tabone, C.J., Florman, J., Ji, H., Greenwood, J., et al. (2016). Pan-neuronal imaging in roaming Caenorhabditis elegans. Proc. Natl. Acad. Sci. USA *113*, E1082–E1088.

von der Emde, G., Amey, M., Engelmann, J., Fetz, S., Folde, C., Hollmann, M., Metzen, M., and Pusch, R. (2008). Active electrolocation in Gnathonemus petersii: behaviour, sensory performance, and receptor systems. J. Physiol. Paris *102*, 279–290.

Welker, W.I. (1964). Analysis of sniffing of the albino rat. Behaviour *22*, 223–244.

Wen, Q., Po, M.D., Hulme, E., Chen, S., Liu, X., Kwok, S.W., Gershow, M., Leifer, A.M., Butler, V., Fang-Yen, C., et al. (2012). Proprioceptive coupling within motor neurons drives C. elegans forward locomotion. Neuron *76*, 750–761.

White, J.G., Southgate, E., Thomson, J.N., and Brenner, S. (1986). The structure of the nervous system of the nematode Caenorhabditis elegans. Philos. Trans. R. Soc. Lond. B Biol. Sci. *314*, 1–340.

Xu, S., and Chisholm, A.D. (2016). Highly efficient optogenetic cell ablation in C. elegans using membrane-targeted miniSOG. Sci. Rep. *6*, 21271.

Zhang, Y., Lu, H., and Bargmann, C.I. (2005). Pathogenic bacteria induce aversive olfactory learning in Caenorhabditis elegans. Nature *438*, 179–184.

STAR★METHODS

KEY RESOURCES TABLE

REAGENT or RESOURCE	SOURCE	IDENTIFIER
Bacterial and Virus Strains		
Pseudomonas aeruginosa PA14	Kim et al., 2002	N/A
Escherichia coli OP50	Caenorhabditis Genetics Center (CGC)	N/A
Experimental Models: Organisms/Strains		
N2 (Bristol), wild type	CGC	WormBase ID: N2
MT15434 *tph-1(mg280)* II	CGC	WormBase ID: MT15434
MT14984 *tph-1(n4622)* II	CGC	WormBase ID: MT14984
IK705 *njIs10[Pglr-3::gfp]*	CGC	N/A
ZC1448 *yxEx696[Pglr-3::TeTx::mCherry; Punc-122::dsRed]*	Hendricks et al., 2012; This study	N/A
ZC1508 *yxIs19[Pglr-3a::GCaMP3, Punc-122::dsred]*	Hendricks et al., 2012	N/A
ZC1598 *eat-4(ky5)* III; *yxIs19*	Hendricks et al., 2012	N/A
ZC1744 *yxIs19; yxEx902[Pttx-3::TeTx::mCherry; Punc-122::gfp]*	This study	N/A
ZC1792 *gar-3(gk305) V*; *yxIs19*	Hendricks et al., 2012	N/A
ZC1923 *gar-3(gk305) V; yxIs19; yxEx968[Pglr-3::gar-3; Punc-122::gfp]*	Hendricks et al., 2012	N/A
ZC2632 *yxIs19; yxIs34[Pceh-36Δ::Caspase-3(p12)::nz;Pceh-36Δ::cz::Caspase-3(p17); Psrtx-1::gfp; Punc-122::dsRed]*	This study; Beverly et al., 2011	N/A
ZC2702 *ttx-3(mg158) X*; *yxIs19*	This study	N/A
ZC2719 *yxIs19; yxEx398[Pglr-3::mCherry; Punc-122::gfp]*	This study	N/A
CX16155 *kyIs640[Pglr-3::GCaMP5a; Pmyo-3::mCherry]*	Jin et al., 2016	N/A
ZC2704 *acc-2(ok2216) IV*; *kyIs640*	This study	N/A
ZC2717 *acc-2(ok2216) IV*; *kyIs640; yxEx1397[Pglr-3::acc-2; Punc-122::gfp]*	This study	N/A
ZC2785 *yxEx1438[Pglr-3::miniSOG(103L)-vamp2-mCherry; Pelt-2::gfp]*	This study	N/A
ZC2786 *yxEx1439[Pglr-3::miniSOG(103L)-mCherry; Pelt-2::gfp]*	This study	N/A
Oligonucleotides		
5′ ttatgctagcATGATATTTACTCTTTTATCAACA 3′	This study	*acc-2* cDNA
5′ aaccggtaccTTATCCGTCAACTCGATT 3′	This study	*acc-2* cDNA
Recombinant DNA		
Pttx-3::TeTx::mCherry	This study	N/A
Pglr-3::TeTx::mCherry	This study	N/A
Pglr-3::miniSOG(103L)-vamp2-mCherry	This study	N/A
Pglr-3::miniSOG(103L)-mCherry	This study	N/A
Software and Algorithms		
Methods S1.rar - customized codes for image collection and analysis	This study	Methods S1

CONTACT FOR REAGENT AND RESOURCE SHARING

Further information and requests for resources and reagents should be directed to and will be fulfilled by the Lead Contact, Yun Zhang (yzhang@oeb.harvard.edu).

EXPERIMENTAL MODEL AND SUBJECT DETAILS

Caenorhabditis elegans strains were cultivated under the standard condition (Brenner, 1974). Adult hermaphrodites are used in this study. The strains used in this study include: N2 (Bristol), MT15434 *tph-1(mg280)* II, MT14984 *tph-1(n4622)* II, IK705 *njIs10 [Pglr-3::gfp]*, ZC1448 *yxEx696 [Pglr-3::TeTx::mCherry; Punc-122::dsRed]*, ZC1508 *yxIs19[Pglr-3::GCaMP3, Punc-122::dsred]*,

ZC1598 *eat-4(ky5)*III; *yxIs19*, ZC1744 *yxIs19; yxEx902[Pttx-3::TeTx::mCherry; Punc-122::gfp]*; ZC1792 *gar-3(gk305)V*; *yxIs19*, ZC1923 *gar-3(gk305)V; yxIs19; yxEx968[Pglr-3::gar-3; Punc-122::gfp]*, ZC2632 *yxIs19; yxIs34[Pceh-36Δ::Caspase-3(p12)::nz;Pceh-36Δ::cz::Caspase-3(p17);Psrtx-1::gfp; Punc-122::dsRed]*, ZC2702 *ttx-3(mg158)X*; *yxIs19*, ZC2719 *yxIs19; yxEx398 [Pglr-3::mCherry; Punc-122::gfp]*, CX16155 *kyIs640[Pglr-3::GCaMP5a; Pmyo-3::mCherry]*, ZC2704 *acc-2(ok2216)IV*; *kyIs640*, ZC2717 *acc-2(ok2216)IV*; *kyIs640; yxEx1397[Pglr-3::acc-2; Punc-122::gfp]*, ZC2785 *yxEx1438[Pglr-3::miniSOG(103L)-vamp2-mCherry; Pelt-2::gfp]*, ZC2786 *yxEx1439[Pglr-3::miniSOG(103L)-mCherry; Pelt-2::gfp]*.

METHOD DETAILS

Transgenes and transgenic animals

To generate *Pttx-3::TeTx::mCherry,* a 0.9 kb sequence upstream of the *ttx-3* gene, which was expressed specifically in the interneuron AIY (Hobert et al., 1997), was generated by polymerase chain reaction (PCR) and cloned into the pCR8 Gateway entry vector (Invitrogen) and the recombination with the destination vector *pSMrfB-TeTx:mCherry* (Hendricks et al., 2012) was performed with the manufacturer's guidelines. To generate *Pglr-3::acc-2*, the coding sequence of *acc-2* was generated by PCR (forward primer 5′ ttatg ctagcATGATATTTACTCTTTTATCAACA, reverse primer 5′ aaccggtaccTTATCCGTCAACTCGATT) using a cDNA library and cloned into a previously generated plasmid containing the promoter region of *glr-3* (Hendricks et al., 2012). The promoter region of *glr-3,* which was known to be expressed specifically in the interneuron RIA (Brockie et al., 2001), was also used to generate *Pglr-3::TeTx::mCherry.* To generate a destination vector of miniSOG, a pair of synthesized oligoes (MCSf 5′-CTAGAccgcgggggagatc tcaatgCTCGAGgggcATCGATggA and MCSr 5′-CCGGTccATCGATgcccCTCGAGcattgagatctccccccgcggT) containing multiple cloning sites were annealed and cloned to the XbaI and the AgeI sites of a plasmid generated by replacing the coding region of *gfp* of the Fire's vector pPD95.77 with a coding sequence of *mCherry*. The new plasmid was named as pYZ001-*mCherry*-MCS. A 1.18kb *glr-3* promoter sequence (Brockie et al., 2001) flanked by SacII and BamHI sites was generated by PCR and cloned into pYZ001-*mCherry*-MCS to generate *Pglr-3::mCherry*. The *miniSOG-vamp2* fragment from the pCR8-miniSOG-vamp2-Citrine plasmid (a gift from John Y. Lin from Lin et al., 2013) flanked by a 5′ EcoRI site and a 3′ ClaI site was cloned into *Pglr-3::mCherry* to generate *Pglr-3::miniSOG-vamp2-mCherry*. Site-directed mutagenesis was performed with Q5 Site-Directed Mutagenesis Kit (New England Biolabs) to generate *Pglr-3::miniSOG(103L)-vamp2-mCherry* (Xu and Chisholm, 2016) (forward primer 5′ CATCGG AGTGCTGCTGGATGG, reverse primer 5′ AAATACTGGAGCTCACCC) following the manufacturer's instruction. The transgenes were injected at 50 ng/μl unless otherwise specified with *Punc-122::gfp* or *Punc-122::dsRed* or *Pelt-2::gfp* as a co-injection marker as previously described (Mello et al., 1991).

Calcium imaging

Calcium imaging with a microfluidic device (Chronis et al., 2007) was performed essentially as described (Hendricks et al., 2012). The fluidic chips were cast using Polydimethylsiloxane and bound to glass coverslips by using a corona treater (Electro-Technic Products, Chicago, IL). The fluidic streams were controlled by an Automate Scientific Valvebank perfusion system (Berkeley, CA). Fluorescence time-lapse imaging was performed on a 40x oil-immersion objective on a confocal Nikon Eclipse Ti-E inverted microscope with an ANODR iXon Ultra EMCCD camera at 5 frames second^{-1}. Image analysis was performed with NIH ImageJ. Briefly, the axonal domains of RIA or other regions of interest (ROI) were manually tracked using ImageJ plugin Manual Tracking to calculate the fluorescence intensity of ROI. The amplitude of head bending was measured with ImageJ. The images were binarized by defining background as 0 and worm as 1. A ROI containing the head was selected and fit to an ellipse. The position where the head and body formed a straight line was defined as the zero degree head bending. The angle between the major axis of an ellipse and the zero degree head bending was the angle of head bending. Ventral direction was positive.

Calcium imaging on freely moving animals were performed on animals that moved on a thin layer of nematode growth medium (1mM CaCl2, 1mM MgSO4, 25mM KPO4 pH6.0, 1.6% Agar) on a cover glass under a 10x objective at 10 frames second^{-1}. The movement of the animal was followed by manually adjusting the position of the XY stage. The images were analyzed using ImageJ, MATLAB, and LabVIEW (National Instruments) scripts (Methods S1). To analyze the fluorescence intensity, the ROI center of each axonal domain was manually tracked using ImageJ plugin Manual Tracking to calculate the fluorescence intensity of ROI. Control experiments for potential effects of movement were performed on transgenic animals that expressed the green fluorescent protein (GFP) specifically in RIA and on transgenic animals that expressed both GCaMP3 and mCherry in RIA (Figure 5). The factors that aid to minimize the potential movement effects include the small size of ROI, the anatomical position of ROI being relatively central to the head of the worm, and the large dynamic range of the GCaMP3 or GCaMP5 signals. To measure the amplitude of head undulations, images were binarized by defining the background as 0 and worm as 1, and skeletonized. The skeletonized images were used to measure head undulations with a customized code (Methods S1). The skeletonized line representing a worm was segmented and anterior segments were used to quantify the amplitude of the head undulation.

Olfactory steering

Locomotion during olfactory steering or in the absence of olfactory cues was recorded on animals moving on a nematode growth medium plate with a Grasshopper3-GS3-U3-120S6M-C camera (FLIR Integrated Imaging Solutions). Under our experimental conditions, the dorsal-ventral undulation occurs at around 0.5 Hz. We recorded locomotory trajectories at 7 frames second^{-1}. Young

adult animals cultivated under the standard condition crawled on an empty NGM plate briefly before being transferred onto a new NGM plate for recording. A drop of 10 μl isoamyl alcohol at specified concentration or 10 μl supernatant of a freshly prepared bacterial culture was used as the odorant source. Bacteria supernatant was prepared by cultivating the *E. coli* strain OP50 or the *Pseudomonas aeruginosa* strain PA14 overnight at 24°C in NGM medium. The worm was initially placed at a position 1.5 cm away from the center of the odorant drop, unless otherwise specified. Recording started a few seconds after the worm was placed on the plate and ended when the worm reached the edge of the drop. Therefore, the traveling distance could be shorter than 1.5 cm. Images were analyzed with the WormLab System (MBF Bioscience). Briefly, to analyze the steering movement, a worm was treated as a point, and the line between two consecutive points was used to define the current direction. The curving angle was determined as previously described (Iino and Yoshida, 2009; Kato et al., 2014) and illustrated in Figure S1. The navigation index was defined and analyzed as previously described (Luo et al., 2014) and as illustrated in Figure 1. The head undulations were identified and measured with the WormLab System (http://www.mbfbioscience.com/wormlab-imaging-system).

Light-induced inactivation with miniSOG

Light-induced inactivation using the miniSOG(103L) fusion protein was performed on an Olympus FV1000MPE microscope under a 20x 1.00 N.A. water immersion objective. Adult transgenic animals expressing *Pglr-3::miniSOG(103L)-VAMP2-mCherry* or *Pglr-3::miniSOG(103L)-mCherry* (untagged control) were immobilized on a thin 5% agar pad with 20 nM sodium azide diluted in Polybead Microspheres (Polysciences). The identification of the RIA axonal domains was aided by the expression of *mCherry*. Axonal domains were illuminated using a 488nm laser for 6-8 minutes. After illumination, the animals were recovered under the standard cultivation condition for 5 minutes before examination of the locomotory behavior. The angles of head undulations were measured using the WormLab System (http://www.mbfbioscience.com/wormlab-imaging-system) and the ventral direction was defined as positive. The average angle of all the head undulations was determined for each worms and multiple worms were examined for each genotype.

Aversive olfactory training and learning assay

The training of adult *C. elegans* with the *P. aeruginosa* strain PA14 and the testing of olfactory learning was performed essentially as previously described (Jin et al., 2016). The synchronized adult hermaphrodite animals were trained by feeding on PA14 for 6-10 hours, after being cultivated on the *E. coli* OP50 lawns. The control and the trained animals were tested on 10 cm chemotaxis assay plates (1mM CaCl2, 1mM MgSO4, 5mM KPO4 pH6.0, 1.6% Agar) that each contained two 20 μl drops of freshly prepared overnight culture of PA14 or OP50, which were diluted to optical density 600 = 1, on the opposite sides of the plate. The worms, after washing with M9 buffer, were placed in the center of the assay plate, equidistant from the two bacterial spots to test their olfactory preference between the two bacterial spots.

QUANTIFICATION AND STATISTICAL ANALYSIS

The boxplots were generated with http://shiny.chemgrid.org/boxplotr/. The statistical tests, value of n and what each n value represents, and other related measures are shown in the legend of each relevant figure. In all, *** $p < 0.001$, ** $p < 0.01$, * $p < 0.05$, N.S., not significant.

DATA AND SOFTWARE AVAILABILITY

Customized codes are provided in Methods S1.